Alma Mater Studiorum · Università di Bologna

Scuola di Scienze
Corso di Laurea Magistrale in Fisica

Dynamics of the Heisenberg XXZ Model across the Ferromagnetic Transition

Relatore:

Prof.ssa Elisa Ercolessi

Presentata da:

Alessandro Cinnirella

Correlatori:

Prof. Fabio Ortolani
Dott. Piero Naldesi

Sessione II

Anno Accademico 2014/2015

Abstract

In questa tesi viene presentata un'analisi numerica dell'evoluzione dinamica del modello di Heisenberg XXZ, la cui simulazione è stata effettuata utilizzando l'algoritmo che va sotto il nome di DMRG. La transizione di fase presa in esame è quella dalla fase paramagnetica alla ferromagnetica: essa viene simulata in una catena di 12 siti per vari tempi di *quench*. In questo modo si sono potuti esplorare diversi regimi di transizione, da quello istantaneo al quasi-adiabatico. Come osservabili sono stati scelti l'entropia di entanglement, la magnetizzazione di mezza catena e lo spettro dell'entanglement, particolarmente adatti per caratterizzare la fisica non all'equilibrio di questo tipo di sistemi. Lo scopo dell'analisi è tentare una descrizione della dinamica fuori dall'equilibrio del modello per mezzo del meccanismo di Kibble-Zurek, che mette in relazione la sviluppo di una fase ordinata nel sistema che effettua la transizione quantistica alla densità di difetti topologici, la cui legge di scala è predicibile e legata agli esponenti critici universali caratterizzanti la transizione.

Contents

Chapter 1

Introduction

In the past decades several efforts have been made in the scientific community in order to explore a variety of many-body models. These models give the opportunity to describe different systems with a relatively simple mathematical construction and deep physical meaning. Interest in this kind of research is mainly growing in condensed matter areas, strongly enhanced by recent developments of powerful experimental techniques based on cold atoms, that allow to create low-dimensional systems exhibiting genuinely quantum properties. Hence, in the present moment we are experiencing an outstanding technical opportunity to test the condensed-matter theoretical predictions as never before. The deep changes occurred in the relationship between theory and experiment rather appear as a role reversal: while in the past semplified models were used to to describe the low-energy physics of more complex systems, nowadays these models can be artificially recreated and their properties broadly investigated.

In this stimulating context, attention has always been devoted to quantum phase transitions, both for their presence in almost all physics area and non-trivial physical description. Indeed, while a comprehensive understanding of quantum phase transitions by means of equilibrium quantities and properties has been reached, the area of non-equilibrium dynamics in closed interacting systems is relatively unexplored. Far from equilibrium, describing the dynamics in complex systems via simplified modesl is not an obvious task. Thus, it is of fundamental importance to investigate whether it is possible to describe the nonequilibrium dynamics of quantum models, i.e. find suitable quantities and protocols that can mark quantum phase transitions and unveal related universal behaviours.

In recent years, with the advent of quantum information the idea of entanglement has been gradually pointed to as a source of correlations giving rise to the various phases of matters. For this reason, new research efforts concen-

trate on describing quantum system in general - and quantum phase transitions particularly - with the help of appropriate quantifiers of entanglement, such as the entanglement entropy. This concepts lead to a deeper understanding of non-equilibrium dynamics, also. For instance, among the various aspects of dynamics in phase transitions, a central role is played by the adiabatic dynamics. In this context, the Kibble-Zurek mechanism manages to relate the ordering in symmetry-breaking phase transitions to the formation of topological defects in the final state of the system, which in turn are due to a lack of information trasmission during the symmetry-breaking process.

In this thesis we are concerned with a quite prototypical interacting quantum system, namely the Heisenberg XXZ model. It consists of a one-dimensional spin-1/2 chain, whose interactions show an anisotropy along a specific direction. Letting this anisotropic coupling costant vary induces different ordering in the system, so that three phases can be charachterised: an antiferromagnetic one, an entirely critical paramagnetic and a ferromagnetic region. We will concentrate on the transition from the paramagnetic to the ferromagnetic phase.

Simulations of this system along with its dynamic evolution are carried out via the Density-Matrix Renormalization Group algorithm in its time-dependent version (tDMRG). Hence, we will investigate the model in different quench regimes and analyse numerically some crucial dynamic properties.

This preliminary work can be thought of as a natural extension of the study on the Ising model carried out in [9], where the single-point quantum phase transition was characterized via the Kibble-Zurek mechanism. We try to apply their description of a non-interacting model to a fully interacting quantum system. The performed analysis is preliminar and hence mainly qualitative, though not lacking of interesting physical meaning.

The outline of this work is the following. Chapter 2 is devoted to the description of the XXZ model from an analytical point of view via the Bethe Ansatz. The phase diagram of the model is deeply outlined, along with the ground states of the different phases. In Chapter 3 we introduce the concept of entanglement entropy, both with its static and dynamic properties, with particular regard to the possibility of use it as a transition marker. Then we illustrate the Kibble-Zurek mechanism in the context of non-equilibrium dynamics of phase transitions. At the end, a broad rewiew on its application in the Ising model is provided. In Chapter 4 attention is focused on the DMRG algorithm, along with its time-dependent counterpart. In the last section, we present some static simulations of the XXZ model, which were primarily used to set up the best configuration both for the system and the DMRG parameters. The last Chapter presents the new results for the dynamics of the XXZ-model ferromagnetic phase transition.

Chapter 2

The Heisenberg Anisotropic Chain

2.1 Overview

The model we will focus on in the present work is the one-dimensional spin-1/2 XXZ model, which is strongly correlated. In the early years of the last century Heisenberg started with a simplified version [21] accounting for the interaction between neighbouring spins: his picture provided a first microscopic motivation for ferromagnetic order. This model also became known as the spin-1/2 isotropic Heisenberg model or XXX model (because of the isotropic interactions in $\hat{x}$, $\hat{y}$ and $\hat{z}$ directions). The Heisenberg chain was then more and more extended introducing different exchange couplings. In the absence of magnetic field, the most general Hamiltonian of spin-1/2 Heisenberg chain with nearest-neighbour interaction is

$$\mathcal{H} = -\frac{1}{2}\sum_{i=1}^{N}[J_x S_i^x S_{i+1}^x + J_y S_i^y S_{i+1}^y + J_z S_i^z S_{i+1}^z]. \tag{2.1}$$

There are four basic combinations for the coupling constants:

- $J_x = J_y = J_z = J > 0$: The isotropic ferromagnetic XXX Heisenberg chain, analytically solved by Bethe [5] in 1931.
- $J_x = J_y = J_z = J < 0$: The isotropic antiferromagnetic XXX Heisenberg chain, whose ground-state energy was obtained by Hulthén [22] in 1938 while its elementary excitations were found by des Cloizeaux and Pearson [13] in 1962.

- $(J_x = J_y = J) \neq J_z$: The XXZ Heisenberg chain, solved by Yang and Yang [43, 44, 45] in 1966.
- $J_x \neq J_y \neq J_z$: The fully anisotropic Heisenberg chain, solved by Baxter [2, 3] in 1972.

We shall concentrate on the XXZ Heisenberg chain.

2.2 The XXZ Heisenberg chain

The spin-1/2 one-dimensional Heisenberg XXZ model with N sites with periodic boundary conditions $\mathbf{S}_{N+j} = \mathbf{S}_j$ is described by the Hamiltonian

$$\mathcal{H} = -J \sum_{i=1}^{N} \{S_i^x S_{i+1}^x + S_i^y S_{i+1}^y + \Delta S_i^z S_{i+1}^z\} - 2h \sum_{i=1}^{N} S_i^z \tag{2.2}$$

where $S_i^\alpha = \frac{1}{2}\sigma_i^\alpha$ and the σ^α are the usual Pauli matrices obeying canonical $SU(2)$ commutation relations

$$\sigma^x = \begin{pmatrix} 0 & 1 \\ 1 & 0 \end{pmatrix} \qquad \sigma^y = \begin{pmatrix} 0 & i \\ -i & 0 \end{pmatrix} \qquad \sigma^z = \begin{pmatrix} 1 & 0 \\ 0 & -1 \end{pmatrix}. \tag{2.3}$$

In Hamiltonian (2.2) the last term accounts for a magnetic field h applied along the $\hat{z}$ direction. The parameter J sets the energy scales. For $J > 0$ ferromagnetic order is preferred in the $\hat{x}$-$\hat{y}$ plane, while for $J < 0$ the ground state of the Hamiltonian exhibits antiferromagnetic alignement.

Parameter Δ quantifies the strength of the uniaxial anisotropy along the $\hat{z}$ direction, which competes with the $\hat{x}$-$\hat{y}$ term. Two regimes can be distinguished in this model: an axial one for $|\Delta| > 1$ and a planar one for $|\Delta| < 1$. In the axial regime, if $J\Delta > 0$ ferromagnetic order along the $\hat{z}$ axis is preferred, while for $J\Delta < 0$ the ground state. The special cases $\Delta = 1$ and $\Delta = -1$ correspond to the ferromagnetic and antiferromagnetic isotropic Heisenberg chains. The model shows several symmetries that can be used in order to evaluate its ground state and low energy excitations. First of all, for an even number of sites, we can transform $\mathcal{H}$ using the unitary operator $V = exp(i\pi \sum_{n=1}^{N} n S_n^z)$

$$V\mathcal{H}(\Delta)V^\dagger = -\mathcal{H}(-\Delta). \tag{2.4}$$

The energy spectra of $\mathcal{H}(\Delta)$ and $\mathcal{H}(-\Delta)$ are related by a reflection around E=0. Thus, the eigenstates of the Hamiltonian are independent from the sign of J, but their energetic order is exactly reverted upon changing of sign. In addition, the magnetisation along the $\hat{z}$ axis, i.e.

$$S^z = \frac{1}{2}\sum_{j=1}^{N} S_j^z \tag{2.5}$$

is conserved. In a configuration with all spins up, it reaches its maximum value $S^z_{\max} = N/2$. Hence, we can focus on the case $0 \leq S^z < N/2$ only, as a rotation along the $\hat{x}$ axis with $h \to -h$ leaves the Hamiltonian unchanged. Moreover

$$[\mathcal{H}, S^z] = 0, \tag{2.6}$$

so we can treat Hilbert space sectors of fixed magnetisation separately.

A further step in the analysis is the introduction of the spin-flip operators in order to make calculations more convenient to deal with. Namely,

$$S_j^+ = S_j^x + iS_j^y, \qquad S_j^- = S_j^x - iS_j^y \tag{2.7}$$

whose action raises or lowers spin states:

$$S^+ |\downarrow\rangle = |\uparrow\rangle \quad S^+ |\uparrow\rangle = 0 \qquad S^- |\uparrow\rangle = |\downarrow\rangle \qquad S^- |\downarrow\rangle = 0. \tag{2.8}$$

Spin commutation relations read: $[S_j^z, S_{j'}^{\pm}] = \pm S_j^{\pm}\delta_{jj'}$ and $[S_j^+, S_{j'}^-] = 2S_j^z\delta_{jj'}$. Using (2.7), Hamiltonian (2.2) becomes

$$\mathcal{H} = -\frac{J}{2}\sum_{j=1}^{N}\{S_i^+ S_{i+1}^- + S_i^- S_{i+1}^+ + 2\Delta S_i^z S_{i+1}^z\} - 2h\sum_{j=1}^{N} S_i^z. \tag{2.9}$$

In 1931 Bethe provided the exact solution for this model in a work that introduced for the first time the powerful analytical technique known as Bethe Ansatz. Nowadays several numerical approaches are more suitable to tackle many-body problems, but the Bethe Ansatz is an important tool from a didactic point of view, because it provides a completely analytical and, at the same time, non-trivial solution of the model.

2.3 The Bethe Ansatz

We start with the state $|0\rangle \equiv |\uparrow\uparrow \dots\rangle$ with all spins pointing up (it may not be the lowest energy state). This state is defined by $S_j^+ |0\rangle = 0$ with $j = 1, \dots, N$. Hamiltonian (2.9) acting on this state gives $\mathcal{H}|0\rangle = E_0 |0\rangle$ with

$$E_0 = -\Big(\frac{J}{4}\Delta + h\Big)N. \tag{2.10}$$

A generic state with r flipped spins can be written as

$$\Psi = \sum_{\{n_l\}} f(n_1, \ldots, n_r) \, |n_1, \ldots, n_r\rangle \tag{2.11}$$

where the sum is performed over all r possible choices of N lattice sites. Also

$$|n_1, \ldots, n_r\rangle = S^-_{n_1} \ldots S^-_{n_r} \, |0\rangle \tag{2.12}$$

indicates the state with r flipped spins at lattice sites n_l. The magnetisation of this site is $S^z = N/2 - r$ and we consider an ordered set of chain sites, i.e. $r \leq N/2$ and $1 \leq n_1 < \cdots < n_r \leq N$. Clearly, for an even number of lattice sites a $SU(2)$ invariant state can appear, i.e. $S^z = 0$ for $r = N/2$. On the other hand, an odd N provides half-integer magnetisation. Applying the Hamiltonian (2.9) on the state (2.11) will result in an eigenvalue equation:

$$\begin{aligned}
&(\mathcal{H} - E)\Psi = \\
&= -\frac{J}{2} \sum_{j=1}^{r} (1 - \delta_{n_j+1, n_{j+1}}) \big[f(n_1, \ldots, n_j + 1, n_{j+1}, \ldots, n_r) + \\
&+ f(n_1, \ldots, n_j, n_{j+1} - 1, \ldots, n_r) \big] + \\
&+ \Big[E_0 - E + (J\Delta + 2h) r - J\Delta \sum_{j=1}^{r} \delta_{n_j+1, n_{j+1}} \Big] f(n_1, \ldots, n_r) = 0.
\end{aligned} \tag{2.13}$$

We now concentrate on the Bethe Ansatz, assuming that the coordinate wave function can be written as a superposition of plane waves, i.e.

$$f(n_1, \ldots, n_r) \equiv \sum_{\mathcal{P}=1}^{r!} A_{\mathcal{P}} \exp \Big[i \sum_{j=1}^{r} k_{\mathcal{P}j} n_j \Big] \tag{2.14}$$

where $\mathcal{P}$ is a permutation of the indices. This *ansatz* automatically satisfies the Schrödinger equation if there are not nearest-neighbour sites with both spins down. When two of the sites in the sequence $n_1, \ldots, n_r$ are nearest neighbours, such as $n_{j+1} = n_j + 1$, we have a sort of consistency equation reading

$$\begin{aligned}
f(n_1, \ldots, n_j + 1, n_j + 1, \ldots, n_r) - 2\Delta f(n_1, \ldots, n_j, n_j + 1, \ldots, n_r) + \\
+ f(n_1, \ldots, n_j, n_j, \ldots, n_r) = 0.
\end{aligned} \tag{2.15}$$

Inserting here the Bethe Ansatz (2.14), we get

$$\sum_{\mathcal{P}=1}^{r!} A_{\mathcal{P}}\left[e^{i(k_{\mathcal{P}j}+k_{\mathcal{P}(j+1)})} - 2\Delta e^{ik_{\mathcal{P}(j+1)}} + 1\right]\cdot$$
$$\cdot\, e^{ik_{\mathcal{P}1}n_1+\cdots+i(k_{\mathcal{P}j}+k_{\mathcal{P}(j+1)})n_j+\cdots+ik_{\mathcal{P}r}n_r} = 0. \quad (2.16)$$

In this summation, $\mathcal{P} = (\mathcal{P}1, \ldots, \mathcal{P}j, \mathcal{P}(j+1), \ldots, \mathcal{P}r)$ is related to $\mathcal{P}_{j,j+1} = (\mathcal{P}1, \ldots, \mathcal{P}(j+1), \mathcal{P}j, \ldots, \mathcal{P}r)$ with $\mathrm{sign}(\mathcal{P}) = -\mathrm{sign}(\mathcal{P}_{j,j+1})$. Evaluating the resulting cancellations and with a little algebra we get

$$A_{\mathcal{P}} = \exp\left[\frac{i}{2}\sum_{j<l}^{r} \tilde{\Theta}(k_{\mathcal{P}j}, k_{\mathcal{P}})\right] \quad (2.17)$$

where $\tilde{\Theta}(k_{\mathcal{P}j}, k_{\mathcal{P}})$ will be evaluated in a moment. Clearly, the relative amplitudes $A_{\mathcal{P}}$ have unit modulus and can be considered as a scattering phase. Thus, we have

$$f(n_1, \ldots, n_r) = \sum_{\mathcal{P}=1}^{r!} \exp\left[i\sum_{j=1}^{r} k_{\mathcal{P}j}n_j + \frac{i}{2}\sum_{j<l}^{r} \tilde{\Theta}(k_{\mathcal{P}j}, k_{\mathcal{P}l})\right]. \quad (2.18)$$

We have an eigenfunction of (2.13) with eigenvalue

$$\begin{aligned} E &= E_0 + \sum_{l=1}^{r}[J(\Delta - \cos k_l) + 2h] \\ &= E_0 + (J\Delta + 2h)r - J\sum_{l=1}^{r}\cos k_l \end{aligned} \quad (2.19)$$

only if

$$A_{\mathcal{P}} = (-1)^{\mathcal{P}}\prod_{j<l}\left(e^{i(k_{\mathcal{P}j}+k_{\mathcal{P}l})} + 1 - 2\Delta e^{ik_{\mathcal{P}j}}\right) \quad (2.20)$$

or, equivalently,

$$e^{i\tilde{\Theta}(k,k')} = -\frac{e^{i(k+k')} + 1 - 2\Delta e^{ik}}{e^{i(k+k')} + 1 - 2\Delta e^{ik'}} \quad (2.21)$$

which means fixing the scattering phase as

$$\begin{aligned}\Theta(k,k') &\equiv \tilde{\Theta}(k,k') - \pi \\ &= 2\arctan\frac{\Delta\sin\frac{1}{2}(k-k')}{\cos\frac{1}{2}(k-k') - \Delta\cos\frac{1}{2}(k-k')}.\end{aligned} \tag{2.22}$$

We can then apply periodic boundary conditions, i.e. $f(n_1,\ldots,n_{r-1},N+1) = f(1,n_1,\ldots,n_{r-1})$, obtaining quantization conditions:

$$\begin{aligned}e^{ik_jN} &= \prod_{j\neq l} e^{i\tilde{\Theta}(k,k')} \\ &= (-1)^{r-1}\prod_{j\neq l}\frac{e^{i(k_j+k_l)} + 1 - 2\Delta e^{ik_j}}{e^{i(k_j+k_l)} + 1 - 2\Delta e^{ik_l}}, \qquad j = 1,\ldots,r.\end{aligned} \tag{2.23}$$

Thus, the wave numbers $k_1,\ldots,k_r$ are quantized according to the fundamental set of r coupled Bethe equations

$$k_jN = 2\pi\tilde{I}_j - \sum_{l=1}^{r}\Theta(k_j,k_l), \qquad j = 1,\ldots,r \tag{2.24}$$

where the $\tilde{I}_j$ are integers (for odd M) or half-integer (for even M) quantum numbers defining the states. Only solutions with distinct wave numbers are allowed to avoid the nullity of the wavefunction.

2.4 Parametrization

The general property of factorization in the scattering phase can be highlighted with a simple reparametrization of the quasi-momenta, achieved by introducing the rapidity λ: in this way the Θ-function will depend on the difference of the corresponding rapidities, i.e. $\Theta(k_j,k_l) = \theta(\lambda_j - \lambda_l)$. The parametrization depends on the value of the anisotropy parameter Δ: for this reason it is convenient to treat separately the regions $\Delta > 1$, $-1 < \Delta < 1$, $\Delta < -1$

1. Ferromagnet $\Delta > 1$: we set $\Delta = \cosh\phi$ $(0 < \phi < \infty)$ and parametrize

$$e^{ik} = \frac{\sin\frac{\phi}{2}(\lambda+i)}{\sin\frac{\phi}{2}(\lambda-i)}. \tag{2.25}$$

In this way, the scattering phase (2.21) becomes

$$-e^{i\tilde{\Theta}(k,k')} = \frac{\sin\left[\frac{\phi}{2}(\lambda-\lambda'+2i)\right]}{\sin\left[\frac{\phi}{2}(\lambda-\lambda'-2i)\right]}. \tag{2.26}$$

Using this relation with the Bethe equations we get

$$\left[\frac{\sin\left[\frac{\phi}{2}(\lambda_j+i)\right]}{\sin\left[\frac{\phi}{2}(\lambda_j-i)\right]}\right]^N=\prod_{l=1(\neq j)}^{r}\frac{\sin\left[\frac{\phi}{2}(\lambda_j-\lambda_l+2i)\right]}{\sin\left[\frac{\phi}{2}(\lambda_j-\lambda_l-2i)\right]},\qquad j=1,\ldots,r. \tag{2.27}$$

The related unnormalized coefficients (2.17) are

$$A_{\mathcal{P}}=\prod_{j<l}\sin\frac{\phi}{2}(\lambda_{\mathcal{P}j}-\lambda_{\mathcal{P}l}+2i). \tag{2.28}$$

2. Isotropic ferromagnet $\Delta=1$: for $\Delta>1$ ϕ is real, while it becomes imaginary for $\Delta<1$. This point can be found by continuity and the parametrization needed is

$$e^{ik}=\frac{\lambda+i}{\lambda-i},\qquad -e^{i\tilde{\Theta}(k,k')}=\frac{\lambda-\lambda'+2i}{\lambda-\lambda'-2i}. \tag{2.29}$$

Thus, Bethe equations read

$$\left[\frac{\lambda_j+i}{\lambda_j-i}\right]^N=\prod_{l=1(\neq j)}^{r}\frac{\lambda_j-\lambda_l+2i}{\lambda_j-\lambda_l-2i},\qquad j=1,\ldots,r \tag{2.30}$$

and A-coefficients are

$$A_{\mathcal{P}}=\prod_{j<l}(\lambda_{\mathcal{P}j}-\lambda_{\mathcal{P}l}+2i). \tag{2.31}$$

3. Paramagnet $|\Delta|<1$: in this case, the angle ϕ is purely imaginary. Therefore, we introduce the real angle γ defined by $\Delta=-\cos\gamma$ with $0<\gamma<\pi$. Thus

$$e^{ik}=\frac{\sinh\frac{\gamma}{2}(\lambda+i)}{\sinh\frac{\gamma}{2}(\lambda-i)} \tag{2.32}$$

that is equivalent to

$$k(\lambda)=2\arctan\left[\frac{\tanh(\gamma\lambda/2)}{\tan(\gamma/2)}\right]\equiv\theta(\lambda|\gamma/2). \tag{2.33}$$

The scattering phase is given by

$$-e^{i\tilde{\Theta}(k,k')}=\frac{\sinh\left[\frac{\gamma}{2}(\lambda-\lambda'+2i)\right]}{\sinh\left[\frac{\gamma}{2}(\lambda-\lambda'-2i)\right]} \tag{2.34}$$

or

$$\tilde{\Theta}(k,k') = 2\arctan\left[\frac{\tanh\left[\gamma(\lambda-\lambda')/2\right]}{\tan\gamma}\right] \equiv \theta(\lambda-\lambda'|\gamma). \tag{2.35}$$

Correspondently, the Bethe equations are

$$\left[\frac{\sinh\left[\frac{\gamma}{2}(\lambda_j+i)\right]}{\sinh\left[\frac{\gamma}{2}(\lambda_j-i)\right]}\right]^N = \prod_{l=1(\neq j)}^{r} \frac{\sinh\left[\frac{\gamma}{2}(\lambda_j-\lambda_l+2i)\right]}{\sinh\left[\frac{\gamma}{2}(\lambda_j-\lambda_l-2i)\right]}, \qquad j=1,\ldots,r \tag{2.36}$$

or

$$N\theta(\lambda|\gamma/2) = 2\pi I(\lambda) + \sum_{\lambda'}\theta(\lambda-\lambda'|\gamma). \tag{2.37}$$

The A-coefficients read

$$A_{\mathcal{P}} = \prod_{j<l}\sinh\frac{\gamma}{2}(\lambda_{\mathcal{P}j}-\lambda_{\mathcal{P}l}-2i). \tag{2.38}$$

4. Isotropic antiferromagnet $\Delta=-1$: similarly to the isotropic ferromagnetic point, it is defined by continuity. The parameter ϕ goes from purely imaginary to complex. The needed parametrization is

$$e^{ik} = \frac{i-\lambda}{i+\lambda}, \qquad k(\lambda) = 2\arctan(2\lambda) \equiv \theta(2\lambda|0). \tag{2.39}$$

The scattering phase is given by

$$-e^{i\tilde{\Theta}(k,k')} = \frac{\lambda-\lambda'-2i}{\lambda-\lambda'+2i}, \qquad \tilde{\Theta}(k,k') = 2\arctan(\lambda-\lambda') \equiv \theta(\lambda-\lambda'|0). \tag{2.40}$$

The Bethe equations read

$$\left[\frac{i-\lambda_j}{i+\lambda_j}\right]^N = \prod_{l=1(\neq j)}^{r}\frac{\lambda_j-\lambda_l-2i}{\lambda_j-\lambda_l+2i}, \qquad j=1,\ldots,r \tag{2.41}$$

or, equivalently,

$$N\theta(2\lambda|0) = 2\pi I(\lambda) + \sum_{\lambda'}\theta(\lambda-\lambda'|0). \tag{2.42}$$

The A-coefficients are

$$A_{\mathcal{P}} = \prod_{j<l} (\lambda_{\mathcal{P}j} - \lambda_{\mathcal{P}l} - 2i). \tag{2.43}$$

5. Antiferromagnet $\Delta < -1$: we set $\Delta = -\cosh\phi$ $(0 < \phi < \infty)$ and parametrize

$$e^{ik} = \frac{\sin\frac{\phi}{2}(i-\lambda)}{\sin\frac{\phi}{2}(i+\lambda)}, \qquad k(\lambda) = 2\arctan\left[\frac{\tan(\phi\lambda/2)}{\tanh(\phi/2)}\right] \equiv \theta(\lambda|\phi/2). \tag{2.44}$$

The scattering phase is

$$-e^{i\tilde{\Theta}(k,k')} = \frac{\sin\left[\frac{\phi}{2}(\lambda-\lambda'+2i)\right]}{\sin\left[\frac{\phi}{2}(\lambda-\lambda'-2i)\right]}, \tag{2.45}$$

i.e.

$$\tilde{\Theta}(k,k') = 2\arctan\left[\frac{\tan[\phi(\lambda-\lambda')/2]}{\tanh\phi}\right] \equiv \theta(\lambda-\lambda'|\phi). \tag{2.46}$$

The Bethe equations read

$$\left[\frac{\sin\left[\frac{\phi}{2}(i-\lambda_j)\right]}{\sin\left[\frac{\phi}{2}(i+\lambda_j)\right]}\right]^N = \prod_{l=1(\neq j)}^{r} \frac{\sin\left[\frac{\phi}{2}(\lambda_j-\lambda_l-2i)\right]}{\sin\left[\frac{\phi}{2}(\lambda_j-\lambda_l+2i)\right]}, \qquad j = 1,\ldots,r \tag{2.47}$$

or

$$N\theta(\lambda|\phi/2) = 2\pi I(\lambda) + \sum_{\lambda'} \theta(\lambda-\lambda'|\phi). \tag{2.48}$$

The A-coefficients are

$$A_{\mathcal{P}} = \prod_{j<l} \sin\frac{1}{2}(\lambda_{\mathcal{P}j} - \lambda_{\mathcal{P}l} - 2i). \tag{2.49}$$

2.5 The ground state

In the ferromagnetic region $\Delta \geq 1$ the absolute ground state of the XXZ Heisenberg chain corresponds to all spins up, i.e. $r = 0$ and

$$E_0 = -(\frac{J}{4}\Delta + h)N. \tag{2.50}$$

For $\Delta < -1$, as previously derived, the Bethe equations read

$$N\theta(\lambda|\phi/2) = 2\pi I(\lambda) + \sum_{\lambda'} \theta(\lambda - \lambda'|\phi). \tag{2.51}$$

with

$$\theta(\lambda|\phi/2) = 2\arctan\left[\frac{\tan(\phi\lambda/2)}{\tanh(\phi/2)}\right], \qquad \theta(\lambda-\lambda'|\phi) = 2\arctan\left[\frac{\tan[\phi(\lambda-\lambda')/2]}{\tanh\phi}\right]. \tag{2.52}$$

In the thermodynamic limit $N \to \infty$, $r \to \infty$, with fixed density of down spins $m = r/N$, we have a ground state density $R(k)$ for the wave numbers between some limits $-q$ and $+q$. The Bethe equations imply

$$k = 2\pi F(k) + \int_{-q}^{+q} \theta(k - k')R(k')\,dk' \tag{2.53}$$

where

$$F(k) \equiv \frac{I(k)}{N} = \int_0^k R(k')\,dk'. \tag{2.54}$$

We can now introduce the density of rapidities $\rho(\lambda)$ via the relation $\rho(\lambda)\,d\lambda \equiv R(k)\,dk$, i.e. $\rho(\lambda) = R(k)k'(\lambda)$. The distribution function of the λ_j at the lowest energy state should satisfy

$$k(\lambda) = 2\pi f(\lambda) + \int_{-b}^{b} \theta(\lambda - \lambda')\rho(\lambda')\,d\lambda' \tag{2.55}$$

with $f(\lambda) = \int_0^\lambda \rho(\lambda')\,d\lambda'$. Differentiating with respect to λ we have

$$k'(\lambda) = 2\pi\rho(\lambda) + \int_{-b}^{b} \theta'(\lambda - \lambda')\rho(\lambda)\,d\lambda. \tag{2.56}$$

The magnetisation and energy are

$$s^z \equiv \frac{S^z}{N} = \frac{1}{2} - m = \frac{1}{2} - \int_{-b}^{b} \rho(\lambda)\,d\lambda, \tag{2.57}$$

$$e \equiv \frac{E}{N} = -\frac{J\Delta}{4} - h + \int_{-b}^{b} \big[2h - \frac{2\pi J\sinh\phi}{\phi}k'(\lambda)\big]\rho(\lambda)\,d\lambda. \tag{2.58}$$

The integral equation (2.56) is not explicitly solvable for all values of $|b|$, apart from the case of $|b|$ taking the maximal value $|b_0|$ permitted in the range. In such situation, one can use Fourier transform of $\theta'(\lambda-\lambda')$ to derive an explicit solution. We shall indicate with $\hat{G}$ the Fourier transform of $G(\lambda) = \theta'(\lambda)/2\pi$

Again, we can tract separately the different sectors of Δ.

1. Paramagnet $-1 < \Delta = -\cos\gamma < 1$: we have

$$\theta'(\lambda|\gamma) = \frac{\gamma \sin(2\gamma)}{\cosh\gamma\lambda - \cos(2\gamma)}. \tag{2.59}$$

In the paramagnetic region $b_0 = \infty$ and

$$\hat{G}(\omega|\gamma) = \int_{-\infty}^{\infty} e^{-i\omega\lambda} \frac{1}{2\pi} \frac{\gamma \sin(2\gamma)}{\cosh\gamma\lambda - \cos(2\gamma)}\, d\lambda = \frac{\sinh[(\pi - 2\gamma)\omega/\gamma]}{\sinh(\pi\omega/\gamma)}. \tag{2.60}$$

Then the Fourier transform of density is

$$\hat{\rho}_0(\omega) = \frac{\hat{G}(\omega|\gamma/2)}{1 + \hat{G}(\omega|\gamma)} = \frac{1}{2\cosh\gamma}, \qquad \rho_0(\lambda) = \frac{1}{4\cosh(\pi\lambda/2)}. \tag{2.61}$$

The ground state energy per site at $s^z = 0$ reads

$$e = -\frac{J\Delta}{4} - J\frac{\sin\gamma}{\gamma} \int_{-\infty}^{\infty} \frac{\sinh[(\pi - 2\gamma)\omega/\gamma]}{\sinh(\pi\omega/\gamma)\cosh\omega}\, d\omega. \tag{2.62}$$

2. Isotropic antiferromagnet $\Delta = -1$: the Fourier transforms are

$$\hat{G}(\omega|0) = \int_{-\infty}^{\infty} e^{-i\omega\lambda} \frac{1}{\pi} \frac{1}{1+\lambda^2}\, d\lambda = e^{-|\omega|} \tag{2.63}$$

and

$$\hat{\rho}_0(\omega) = \frac{\hat{G}(\omega/2|0)}{1 + \hat{G}(\omega|0)} = \frac{1}{2\cosh\omega}, \qquad \rho_0(\lambda) = \frac{1}{4\cosh(\pi\lambda/2)}. \tag{2.64}$$

Thus

$$e = -J(\ln 2 - \frac{1}{4}). \tag{2.65}$$

3. Antiferromagnet $\Delta = -\cosh\phi < -1$: in this range $b_0 = \pi$ and

$$\theta'(\lambda|\phi) = \frac{\phi \sinh(2\phi)}{\cosh(2\phi) - \cos(\phi\lambda)}. \tag{2.66}$$

Hence, we have

$$\hat{G}(n|\phi) = \int_{-\pi}^{\pi} e^{-in\lambda} \frac{1}{2\pi} \frac{\phi \sinh(2\phi)}{\cosh(2\phi) - \cos(\phi\lambda)} \, d\lambda = e^{-2\phi|n|}. \tag{2.67}$$

For the density of λ_j

$$\hat{\rho}_0(n) = \frac{\hat{G}(n|\phi/2)}{1 + \hat{G}(n|\phi)} = \frac{1}{2\cosh(\phi n)}, \qquad \rho_0(\lambda) = \frac{1}{4\pi} \sum_{n=-\infty}^{\infty} \frac{e^{in\lambda}}{\cosh(\phi n)} = \frac{\mathrm{Kdn}(K\lambda/\pi, u)}{2\pi^2} \tag{2.68}$$

where

$$\mathrm{K} \equiv K(u) = \int_0^{\frac{\pi}{2}} \frac{d\phi}{\sqrt{1 - u^2 \sin^2 \phi}} \tag{2.69}$$

is the complete elliptic integral of the first kind, whose modulus u is related to ϕ through

$$\phi = \pi \frac{K(\sqrt{1-u^2})}{K(u)}. \tag{2.70}$$

Thus we have

$$e = -\frac{J\Delta}{4} - J \sinh\phi \left[\frac{1}{2} + 2 \sum_{n=1}^{\infty} \frac{1}{e^{2n\phi} + 1} \right]. \tag{2.71}$$

2.6 The string solution

By introducing rapidities we restored a sort of translational invariance for the scattering phase. Some states can be characterised only by real rapidities. On the contrary, a great number of admitted states can be related to complex rapidities. Generally, to find them a numerical and maybe difficult approach is required. Anyway, a simple description arises in the thermodynamic limit $N \to \infty$. It is called string hypothesis, as it has not been proved yet that it describes the whole Hilbert space. Two spin waves form a bound state when the total wavefunction decreases exponentially with the distance between them: the bound states of clusters of the flipped spins are the so-called strings. The string contains a group of complex rapidity solutions equispaced symmetrically around the real axis. When the number of down spins r is finite, the Bethe equations imply such strings, which are low-lying excitations from the ground state in the ferromagnetic region $\Delta \geq 1$.

We concentrate on the case $\Delta = 1$ first: in the sector $r = 1$, the Bethe equation (2.30) is

$$e^{ikN} = \left[\frac{\lambda_j + i}{\lambda_j - i}\right]^N = 1. \tag{2.72}$$

In the limit $N \to \infty$ such excitations are called magnons. The energy of a magnon with wave number k is

$$e(k) = J(1 - \cos k). \tag{2.73}$$

When $r = 2$ spins are down, the Bethe equations read

$$\left[\frac{\lambda_1 + i}{\lambda_1 - i}\right]^N = \frac{\lambda_1 - \lambda_2 + 2i}{\lambda_1 - \lambda_2 - 2i}, \qquad \left[\frac{\lambda_2 + i}{\lambda_2 - i}\right]^N = \frac{\lambda_2 - \lambda_1 + 2i}{\lambda_2 - \lambda_1 - 2i}. \tag{2.74}$$

Obviously, this systems exhibits real and complex solutions. In order to concentrate on the real ones first, we set $\lambda_1 - \lambda_2 + 2i/\lambda_1 - \lambda_2 - 2i = \exp(i\vartheta)$, $\vartheta \in \mathbb{R}$. Then $e^{ik_1 N} = e^{i\vartheta}$ and $e^{ik_2 N} = e^{-i\vartheta}$. In the thermodynamic limit we have a state consisting in two independent magnons with total energy

$$e(k_1) + e(k_2) = 2J\left[1 - \cos\left(\frac{k_1 + k_2}{2}\right)\cos\left(\frac{k_1 - k_2}{2}\right)\right]. \tag{2.75}$$

Instead, the complex solution can be described using

$$\lambda_1 = u_1 + iv_1, \qquad \lambda_2 = u_2 - iv_2, \tag{2.76}$$

with u_i and v_i real. Assuming $v_1 > 0$ and with $N \to \infty$, we have $u_1 = u_2 = u$ and $v_1 - v_2 = 1$. Thus, by means of (2.74), we get

$$\left[\frac{u + i(v_1 + 1)}{u + i(v_1 - 3)}\right]^N = 1 \tag{2.77}$$

which leads, again in the thermodynamic limit, to $v_1 = 1$ and $u \in \mathbb{R}$. Consequently, the the $r = 2$ string solution reads

$$\lambda_1 = u + i, \qquad \lambda_2 = u - i \tag{2.78}$$

and it represents the bound state of two magnons with total momentum and energy

$$K = k_1 + k_2 = \frac{1}{i} \ln \left(\frac{u+2i}{u-2i} \right), \tag{2.79}$$

$$E = E_0 + \frac{4J}{u^2+4} + 4h = E_0 + \frac{J}{2}(1 - \cos K) + 4h. \tag{2.80}$$

This energy is always lower than the sum of two independent magnons. Moreover, it is easy to see that the wavefunction amplitude vanishes exponentially as the distance between the flipped spins grows: this evidence marks the enhanced probability to find the spins on neighbouring sites, which exactly corresponds to the definition of bound state.

The same description can be extended to the general r case. All the conditions required are satisfied only if the rapidities form an M-string,

$$\lambda_j = u + i(M + 1 - 2j), \qquad j = 1, \ldots, M. \tag{2.81}$$

Each of them is characterized by total momentum and energy

$$K = \frac{1}{i} \sum_{j=1}^{M} \ln \left(\frac{\lambda_j + i}{\lambda - i} \right) = \frac{1}{i} \ln \left(\frac{u + iM}{u - iM} \right) \tag{2.82}$$

$$E_M = E_0 + \frac{2MJ}{u^2 + M^2} + 2Mh. \tag{2.83}$$

The dispersion relation for these excitations is

$$E_M = E_0 + \frac{J}{M}(1 - \cos K) + 2Mh. \tag{2.84}$$

Now we consider $\Delta > 1$. Recalling $\Delta = \cosh \phi \, (\phi > 0)$ and following the same procedure of the isotropic ferromagnetic case, all the necessary conditions are satisfied only if

$$\lambda_j = u + i(M + 1 - 2j), \qquad j = 1, \ldots, M. \tag{2.85}$$

The total momentum and energy of the M-string are given by

$$K = \frac{1}{i} \sum_{j=1}^{M} \ln \left[\frac{\sin \frac{\phi}{2}(\lambda_j + i)}{\sin \frac{\phi}{2}(\lambda_j - i)} \right] = \frac{1}{i} \ln \left[\frac{\sin \frac{\phi}{2}(u + iM)}{\sin \frac{\phi}{2}(u - iM)} \right], \tag{2.86}$$

$$E = E_0 + \frac{J \sinh \phi \sinh (M\phi)}{\cosh (M\phi) - \cos (\phi)} + 2Mh \tag{2.87}$$

and the dispersion relation is

$$E = E_0 + 2Mh + \frac{J \sinh \phi}{\sinh (M\phi)} \big[\cosh (M\phi) - \cos K\big]. \tag{2.88}$$

For a state with all r flipped spins belonging to a single complex of size $r = M$ and in the limit of $\Delta \gg$ or $\phi \gg$ the energy is

$$E = J\Delta + 2Mh. \tag{2.89}$$

This corresponds to a bound state of M consecutive down spins in a up-spin sea. If Δ is smaller, the lowest energy state for this string solution is the one with zero momentum and we have

$$E = -\frac{J\Delta}{4} N - (N - 2M)h + J \sinh \phi \tanh \left(\frac{M\phi}{2}\right). \tag{2.90}$$

Chapter 3

Entanglement Entropy and Quantum Phase Transitions

3.1 Overview

The development of quantum mechanics in the early decades of the XX$^{\text{th}}$ century led to several concepts standing far beyond common sense. These assertions capture the essence of quantum mechanics in the common imaginary more than any other result, as they express all the innovation brought by the new approach to the physics understanding. The most known of these emblematic achievements can be summarily listed: the existence of a natural uncertainty linked to every measure we cannot in any way overcome, the wave-particle duality which allows particles interference or the quantisation of energy levels.

Nonetheless, one phenomenon is perhaps the most representative and disturbing of quantum mechanics, thence it attracted the attention of physicists since the early stage of the new discipline (see, just to mention, the works by Einstein, Podolsky and Rosen [15] and Schrödinger [38]). In their concerne, the most genuinely and distinctive property of quantum realm is *entanglement*, which can be defined in several ways. Simply put, it implies that a measurement of an observable done on one part of the system may have radical consequences on the possible outcome of a measurement on another part of the system. Indeed, differently from classical correlations that are strictly limited by the speed propagation of signals, entanglement manifests itself instantaneously. For these reasons, it has been pointed [4] as a source of "spooky" non-local connections between subsystems, no matter how far apart in space (for a review, see [1] or [27])

The interest in entangled states has risen dramatically in the last 20 years

with the advent of quantum information theories: in this picture, entanglement is a powerful resource of information deeply investigated [29]. The massive speed-up in quantum computation and communication is based on this property, which is crucial for several quantum protocols also, such as quantum teleportation.

At the same time, entanglement found important applications in areas apparently far apart from quantum information: it is the case of black holes physics, which first borrowed the concept of entanglement to explain the properties of the Hawking's radiation; later on, entanglement introduced a fresh perspective in our understanding of quantum many-body systems. Traditionally, quantum many-body problems are tackled looking at their response to external perturbation fields, order parameters and excitation spectra. Nonetheless, quantum systems are ultimately characterised by the observable correlations they exhibit, which in turn give rise to the various phases of matter (e.g. superconductivity, ferromagnetism, quantum hall systems). This very property suggests a strict link with entanglement, which is nothing but an expression of quantum correlations. The benefit is extended back to quantum information, as the experience built-up in condensed matter areas helps in finding new protocols for quantum computation and communication.

This chapter is structured as follows: first the concept of the Von Neumann entropy as a measure of entanglement is introduced along with its basic properties. Then we give a description of its scaling behaviour, with a brief review of quantum phase transitions and universality hypothesis. Particularly for this section, the theoretical system will not presented as a whole. Instead, we will only focus on the main features that will turn useful in describing the the considered one-dimensional XXZ model. In section 3.4 the non-equilibrium dynamics of entanglement is presented, with the usual protocol for its investigation, i.e. the quantum quench. An overview of the Kibble-Zurek mechanism follows, sketched for both classic and quantum phase transitions. Finally, section 3.6 deeply reviews paper [9], whose content inspired the work of this thesis.

3.2 Entanglement entropy

A simple mathematical definition of entanglement can be given using density matrices: a pure bipartite state is not entangled if and only if it can be written as a tensor product of pure states of the parts. In addition, being A and B partitions of the system, we can take $|\psi_{AB}\rangle$ belonging to $\mathcal{H} = \mathcal{H}_A \otimes \mathcal{H}_B$. According to the Schmidt decomposition, two orthonormal bases $|\varphi_i\rangle_A$ and $|\phi_i\rangle_B$ exist such that we can write the state as

$$|\psi_{AB}\rangle = \sum_{i}^{\chi} \alpha_i \, |\varphi_i\rangle_A \, |\phi_i\rangle_B \tag{3.1}$$

where α_i are positive coefficients and $\chi \leq \min(\min\mathcal{H}_A, \min\mathcal{H}_B)$ is the Schmidt number. This particular basis is just the eigenbasis of the corresponding reduced density operators $\rho_{B/A} = \mathrm{tr}_{A/B}(|\psi_{AB}\rangle) = \sum_i^{\chi} \alpha_i^2 \, |\varphi_i\rangle_{B/A} \, \langle\varphi_i|_{B/A}$. The density operators ρ_A and ρ_B have identical eigenvalues [29].

But how do we quantify the entanglement? In fact, many ways of measuring this quantity are possible (for a comprehensive overview, see [1]), but each one is submitted to the following conditions:

1. local unitary operations are not expected to change entanglement between subsystems. Thus, an entanglement measure must be invariant under such operations, i.e. S must be a function of α_i's only;

2. the measure must be continuous;

3. it must be addictive, that is $S(|\varphi\rangle \otimes |\phi\rangle) = S(|\varphi\rangle) + S(|\phi\rangle)$.

The unique measure satisfying all the above conditions is the Von Neumann entropy of the reduced density matrices (or any monotonic function of it). It is defined as the Shannon entropy of the moduli square of the Schmidt coefficients:

$$S_A = S_B = -\sum_i \alpha_i^2 \log_2 \alpha_i^2. \tag{3.2}$$

Using the reduced density matrices of each part of the system, we can write the previous equation as

$$S_A \equiv S(\rho_A) = -\mathrm{tr}(\rho_A \log_2 \rho_A). \tag{3.3}$$

This is called the *entanglement entropy* of the subsystem A. A remarkable property of this bipartite entropy is that it is not extensive, i.e. $S(A) = S(B)$ and the entropy depends only on the bipartition of the system. This is strictly related to another crucial property known as the area law [16]. It follows from a simple idea: considering a volume containing some general degrees of freedom displaying local interactions, the entanglement of the volume with the outside will be created between the internal and external of such degrees. Thus, the entropy should naturally depend on the area of the surface enclosing the volume, i.e. its scaling is linear in the boundary area of the volume considered.

In one-dimensional systems, consisting of a block of sites arranged on a single line, the boundary is given by one/two sites in case of PBC/OBC. Hence, if the entropy follows an area law, it is expected to scale as a constant [16] independently from the block size as well as the lattice size, that is

$$S(\rho_A) = O(1). \tag{3.4}$$

Whether an area law holds or not, it mainly depends on vicinity of the system to a quantum critical point, as we will see looking at the scaling properties of entanglement entropy.

The most common generalization of the Von Neumann entropy is the *Rényi entropy* (see [29]), defined as

$$S_n(A) = \frac{1}{1-n} \log \mathrm{tr}(\rho_A^n) \tag{3.5}$$

with $n > 0$. For $n \longrightarrow 1$ the Von Neumann entropy is recovered.

Just before introducing the scaling properties of entanglement entropy, it is useful to recall the basic concepts concerning phase transitions with a particular focus on quantum ones (QPT). For the aim of this work only a sketch of the argument will be done at the beginning of the next paragraph. For a complete description see [28] and [36].

3.3 Scaling of the entropy

The Hamiltonian governing the microscopic behaviour of a quantum system results in different macroscopic arrangements, which we call phases, depending on the values of the control parameters. The transition between such phases can be observed looking at an order parameter, i.e. a physical quantity whose value is non-zero in the phase considered and null in the others. The points in the phase diagram which display the change in the order parameter and mark the phase transition are called *quantum critical points* (QCPs): an array of such points is called critical line.

Beneath this description lies the concept of spontaneous symmetry breaking, that can be summarised as follows: a system whose Hamiltonian shows some symmetries can eventually end up in a low-energy state breaking those symmetries, even if the state itself is described by the same invariant equations. In this way, we can have an ordered phase that violates the Hamiltonian symmetry.

Concerning the relationship between classical and quantum behaviour, we know that classical statistic mechanics and fluctuations (typically around $k_B T$) suffice to describe the phase diagram of a system at high temperature, while as the temperature is lowered quantum behaviour starts to become significant. Eventually, quantum fluctuations become prominent and the system behaves in a genuine quantum way. These fluctuations can appear both in space and time and correlation functions for the order parameter can be defined, describing the range of these fluctuations. Near a critical point, the correlation length ξ and

correlation time τ both tend to diverge with a power law that characterise the point itself, i.e.

$$\xi \sim |t|^{-\nu}, \qquad \tau \sim |t|^{-\nu z} \tag{3.6}$$

where ν is the correlation-length critical exponent and z is the dynamic one [36]. From a classical point of view, t is the reduced temperature $(T - T_C)/T_C$, while in the quantum picture we have $(g - g_C)/g_C$, where g is the dimensionless coupling governing the Hamiltonian. The quantum effects obviously propagate even at finite temperature, but only in a delimited range called quantum critical.

A continuous (or second order) quantum phase transition can be often characterised by an energy gap between the ground state and the first excited state. More generally, a relevant energy gap vanishing at the critical point marks the transition in the thermodynamic limit of an infinite system. Consequently, however the critical point is approached varying the Hamiltonian parameters, the system at a certain time cannot follow adiabatically the instantaneous ground state. Thus, excitations arise in the quantum system.

It is evident in this picture how crucial the study of QPT and related QCP is to understand the deep physical processes driving many-body systems. Many scientists devoted a great effort of work to unveil the relation between entanglement and QPT, being the former a measure of the quantum correlations driving the system across phase transitions. Moreover, entanglement entropy can be extremely helpful in this hard task, because it indeed shows a peculiar behaviour allowing to detect QPT.

We saw earlier that in one dimensional systems, if an area law holds, then the scaling of entanglement entropy would be upper bounded independently from the system size. This is exactly the case of gapped systems with finite correlation length. On the contrary, if the correlation length becomes infinite and the system is gapless, we have a violation of the area law and the entanglement entropy diverges logarithmically. Eventually, we can distinguish three main sectors [1] in the behaviour of entanglement entropy:

- Near a quantum critical point the block entropy diverges logarithmically. Being L the length of the system and l the length of the block, with periodic boundary conditions then we have

$$S_l = \frac{c}{3} \log_2 \left[\frac{L}{\pi a} \sin\left(\frac{\pi}{L} l \right) \right] + A \tag{3.7}$$

  where c is the central charge of the underlying conformal field theory we will qualitatively sketch below, a is an ultraviolet regularization cut-off and A is a non-universal constant.

- Away form the critical point, when the system has large but finite correlation length $\xi \gg a$ and the Hamiltonian describes short-range interactions, the entropy saturates to the finite value

$$S_l \sim \frac{c}{3} \log_2 \frac{\xi}{a} \qquad \text{for } l \to \infty. \tag{3.8}$$

- An extension to finite temperature in the critical case has been obtained using conformal field theory with the result:

$$S_l = \frac{c}{3} \log_2 \left[\frac{\beta}{\pi a} \sinh \left(\frac{\pi}{\beta} l \right) \right]. \tag{3.9}$$

This behaviour has been confirmed for different models and situations. A calculation of the block entropy by means of conformal field theory including the case of open and periodic boundary conditions, different partitions, non-critical systems and finite temperature has been performed by Calabrese and Cardy [6]. Starting from the work on the XX model of Jin and Korepin [24], explicit analytic calculations for a number of one dimensional XY spin models have been carried out by Eisler and Zimborás [17], Its *et al.* [23] and Peschel [32], just to mention a few. Numerical calculations on the XX and XXZ models were also performed by De Chiara *et al.* [11] and Laflorencie [25]. Thus, it is proved that entanglement entropy generally obeys a logarithmic scaling equation near a quantum critical point, whereas it reaches saturation away from criticality.

At critical points *universality* manifests itself, as a consequence of the divergence of correlation length [34]. The following tractation is related to low-dimensional systems, as deviation from this general behaviour may arise if dimension grows. Simply put, with the universality hypothesis, i.e. insensitivity to microscopic details, a number of key properties depends only on the universality class of the transition, determined by its space dimension, basic symmetries and range of interactions. Universality can be understood using the renormalization group, which shows that as a system is driven to lower energies and longer length scales, many of the originally describing parameters become irrelevant, while only a few are influent for the low-energy states. Hence, a many-body system undergoing a phase transition becomes phase invariant and can be described in terms of conformal field theories, that describe such models by means of the symmetry of the relative conformal group [7]. Every universality class is identified by the central charge c that appears in Eq. (3.7), (3.8) and (3.9). This quantity in a certain sense quantifies the degrees of freedom of the theory. For free bosons $c = 1$, while for Ising universality class $c = 1/2$.

Summing up, we see that when a one-dimensional system is local and gapped (i.e. there is a length scale provided by the correlation length) the entanglement

entropy saturates to a finite value and we must expect an area law to hold. On the contrary, when a system has long-ranged interactions, the area law may be violated. In any case, the scaling of entanglement entropy can be used as a mark of quantum phase transitions [1, 27].

Ending this section, we recall that boundaries may alter significantly the entanglement entropy [7]. If we have open boundary conditions, the coefficient in Equation (3.7) is one half of the one with periodic conditions, that is

$$S_l = \frac{c}{6}\log_2\left[\frac{2L}{\pi a}\sin\left(\frac{\pi}{L}\,l\right)\right] + \log g + \frac{A}{2} \tag{3.10}$$

with $\log g$ boundary entropy.

3.4 Dynamics of entanglement

The study of *non-equilibrium dynamics* of quantum many-body system has received an impressive boost (for an overview, see [34]) in recent times. New experimental technologies such as cold atomic systems and nanostructures with a high degree of tunability of Hamiltonian parameters make possible a comparison with nonequilibrium theories, which was absolutely unattainable some years ago. At the same time, new numerical algorithms have been developed to carry on simulations of time-evolving quantum systems with an high degree of precision.

One of the simplest and most used protocols allowing to study the non-equilibrium dynamics is the so-called *quantum quench*. First, the system is prepared at $t = 0$ in a pure state $|\psi_0\rangle$ which is the ground state of Hamiltonian $\mathcal{H}_0$, corresponding to an eigenstate λ_0. Then, for $t > 0$, the parameter is suddenly quenched from its initial value to $\lambda \neq \lambda_0$. Generally, $|\psi_0\rangle$ will not be an eigenstate of the new Hamiltonian $\mathcal{H}$. Hence, there will be a non-equilibrium situation, in which the system will evolve unitarily according to the new Hamiltonian.

This kind of situation is particularly interesting when the system is driven through a quantum critical point, with remarkable changes in the state from initial to final point. It was proved [7] that a quench of the system from a non-critical to a critical point leads the block entropy to increase linearly with time up to $t^* = l/2v$ where l is the dimension of the block and v is the spin wave velocity. Eventually, for $t \gg t^*$ the entropy saturates at an asymptotic value. Thus, we have

$$S_l(t) \sim \begin{cases} t & t \leq t^* \\ l & t \geq t^* \end{cases}. \tag{3.11}$$

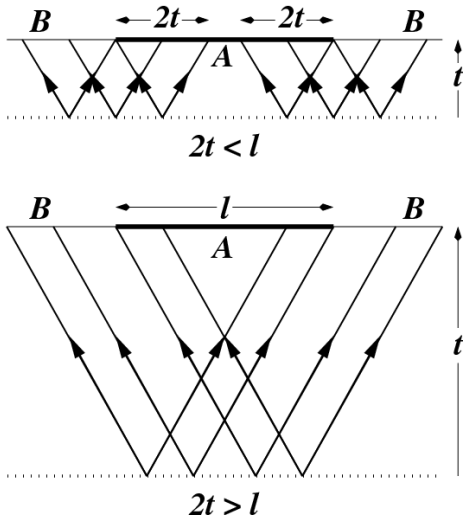

Figure 3.1: Space-time picture illustrating how the entanglement between an interval A and the rest of the system, due to oppositely moving coherent quasiparticles, grows linearly and then saturates.

In [7] a simple explanation of this behaviour is given, based on quasi-particle excitations emitted from the initial state at $t = 0$ and freely propagating with velocity v. The initial state $|\psi_0\rangle$ has a very high energy, relatively to the ground state of the new Hamiltonian $\mathcal{H}$ that drives the system during time evolution. Thus, this former ground state becomes a source of quasi-particle excitations. Particles emitted at the same point of the chain are highly entangled and can move in opposite directions. The entanglement between the block l and the universe at a certain t is related to the number of pairs whose particles belong each one to the different parts of the systems (see Figure 3.1). It is straightforward that the entanglement entropy will increase until the pair created in the middle of the chain reaches its boundary, i.e. until every pair created has one of its entangled particles outside the block.

3.5 The Kibble-Zurek mechanism

As we have seen, both classic and quantum phase transitions are characterised by different ordering on the two sides of the related critical point. Let us consider the behaviour of a classic system driven across a phase transition by the change of a control parameter λ. In second order phase transitions, the change is continuous and the critical point shows a divergence of equilibrium correlation length ξ

$$\xi \sim |\epsilon|^{-\nu}, \tag{3.12}$$

and equilibrium relaxation time τ_r (that describes the reaction time of the system to external perturbations)

$$\tau_r \sim \xi^z. \tag{3.13}$$

In these equations we have defined a dimensionless reduced parameter ϵ measuring the distance from the critical point at a finite temperature T_c:

$$\epsilon = \frac{T - T_c}{T_c}. \tag{3.14}$$

Hence, the symmetry-breaking transition from a high-ordered situation can be expressed in terms of this last parameter. We assume that it varies from negative to positive values movng from order to disorder. In (3.12) ν is the correlation length critical exponent, while z in (3.13) is the dynamic critical exponent. In the context of universality, we can distinguish between different universality classes looking at the critical exponents: different systems belonging to the same class have identical exponents.

The Kibble-Zurek mechanism (KZM) describes the dynamics of a continuous phase transition related to a time-dependent change in the order parameter, driving the system across a critical point (for a review, see [14]). Near the critical point we can consider a linear time-dependence, that is

$$T(t) = T_c[1 - \epsilon(t)]. \tag{3.15}$$

The reduced parameter ϵ is characterised by the *quench time* τ and varies as

$$\epsilon(t) \approx -\frac{t}{\tau}, \tag{3.16}$$

from which we see that the critical point is reached at $t = 0$. This implies that the relative transition rate is $|\epsilon^{-1}\dot{\epsilon}|$ and diverges near the critical point. Thus, we can individuate three regions of different behaviour [12]:

- For $T \gg T_c$, the equilibrium relaxation time is faster than the transition rate. Thus, the behaviour of the system is essentially adiabatic and it can react to every imposed variation.

- In the opposite situation, very close to the critical point for which $\epsilon(t) = 0$, the dynamics is frozen due to the divergence of the equilibrium relaxation time. Simply put, no matter how slow is the quench, at the critical point the evolution ends to behave adiabatically. This happens because at a certain point the order parameter ceases to keep up with the changes in the Hamiltonian, and does not follow its equilibrium value. This is usually known as 'critical slowing down'.

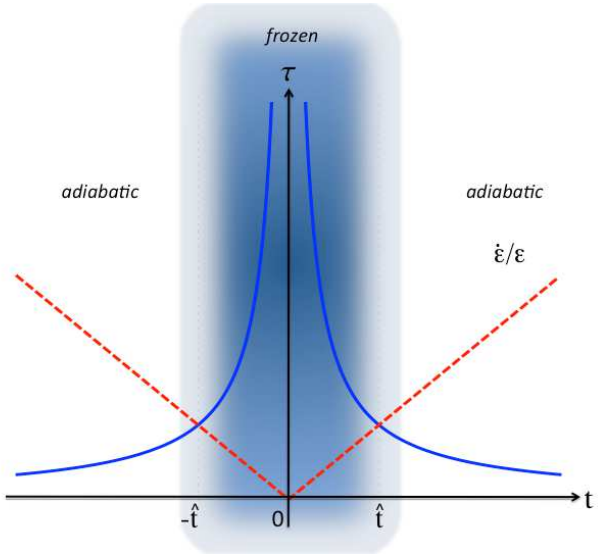

Figure 3.2: Adiabatic-impulse-adiabatic approximation: during a linear quench, the reduced control parameter ϵ forces the system to cross the critical point moving from the high symmetry phase ($t < 0$) to the low symmetry phase ($t > 0$). Due to the divergence of the relaxation time, associated with the critical slowing down near $\epsilon = 0$, the order parameter ceases to follow its equilibrium expectation value and "freezes out" within the time interval $[-\hat{t}, \hat{t}]$.

- For $T \ll T_c$, again far from the critical point, the system returns adiabatic.

This is the so-called *adiabatic-impulse-adiabatic approximation* and represents the essence of the Kibble-Zurek mechanism (see Figure 3.2 for a schematic representation).

The boundary between the adiabatic and impulse regions can be estimated comparing the equilibrium relaxation time and the inverse of the transition rate:

$$\tau_r(t) \approx |\epsilon/\dot{\epsilon}|. \tag{3.17}$$

This yields the time scale characterising the adiabatic-to-impulse crossover, i.e. $t = -\hat{t}$ with

$$\hat{t} = \tau^{\frac{z\nu}{1+z\nu}} \tag{3.18}$$

that corresponds to

$$\hat{\epsilon} \sim \tau^{-\frac{1}{1+z\nu}}. \tag{3.19}$$

At this time, the relevant degrees of freedom cannot follow the externally imposed change of $\epsilon(t)$ and the order parameter "freezes" at the equilibrium value of the adiabatic regime. Thus, the state does not change until $-\hat{\epsilon}$ is

reached: there, the system suddenly "wakes up" in the symmetry broken phase, but it still is in the state of thermal equilibrium for $+\hat{\epsilon}$ in the symmetric phase. Hence, it shows small thermal fluctuations of the order parameter with a finite correlation length

$$\hat{\xi} \sim \hat{\epsilon}^{-\nu} \sim \tau^{\frac{\nu}{1+\nu z}}. \tag{3.20}$$

These fluctuations represent the starting point for the next adiabatic evolution.

Passing $-\hat{\epsilon}$, the system is capable to react to external changes, but the order parameter equilibrium value is no longer zero. The thermal fluctuation initialise the symmetry-breaking process, leading to a structure of ordered domains whose average size is set by $\hat{\xi}$. Even though the order parameter is constant in each domain, different domains are uncorrelated.

Quantum phase transitions at zero temperature are qualitatively different from classic ones, even if the scalings have the same formal description: time evolution is unitary, so no damping is present, and thermal fluctuations are lacking.

Let us consider an isolated quantum critical point between two gapped phases. Both reaction time τ_r and correlation length ξ diverge as

$$\tau_r \sim |\epsilon|^{-z\nu}, \qquad \xi \sim |\epsilon|^{-z\nu} \tag{3.21}$$

where again ϵ measures the distance from the critical point. This time, we can look at a general parameter g in the Hamiltonian driving the transition:

$$\epsilon = \frac{g - g_c}{g_c}. \tag{3.22}$$

The reaction time determines the capability of the system to react to external changes, while the correlation length sets the scale of recover for the order parameter, i.e. the return to the ground state value.

In QCP the time scale is referred to the inverse of the characterising energy gap between ground state and first excited one. This means that

$$\tau_r \simeq \Delta^{-1}. \tag{3.23}$$

As a matter of fact, we have an inferior limit set on the velocity of adiabatic adjustment reacting to external perturbations, expressed by ϵ. Near the critical point the gap vanishes as

$$\Delta \sim |\epsilon|^{\nu z}. \tag{3.24}$$

Considering a second order QPT with reduced parameter given by

$$\epsilon(t) = -\frac{t}{\tau}, \tag{3.25}$$

we can again assume a linearisation near the critical point, i.e.

$$\epsilon(t) \approx \frac{d\epsilon}{dt} t. \tag{3.26}$$

Hence we can identify the quench time as $\tau = |\dot{\epsilon}|^{-1}$ for $\epsilon = 0$.

Again, we have three regions with different behaviour:

- Initially, at $t \longrightarrow -\infty$ the system is in its ground state. During the evolution, as long as the reaction time is fast enough or the gap is large enough, this state evolves adiabatically following ϵ.

- At $t = -\hat{t}$ adiabaticity starts to cease, when the relative transition rate $|\dot{\epsilon}|$ becomes equal to the gap. Hence,

$$\hat{t} \sim \tau^{\frac{\nu z}{1+\nu z}} \tag{3.27}$$

  which corresponds to

$$\hat{\epsilon} \sim \tau^{-\frac{1}{1+\nu z}}. \tag{3.28}$$

  After this time, the evolution becomes impulse and the state freezes out until $+\hat{t}$. In this range the reaction time is too slow and the system cannot follow the evolution of parameter $\epsilon(t)$. Near $-\hat{t}$ the ground state of the system has correlation length

$$\hat{\xi} \sim \hat{\epsilon}^{-\nu} \sim \tau^{\frac{\nu}{1+\nu z}}. \tag{3.29}$$

  In the adiabatic-impulse-adiabatic approximation, this state is frozen between $-\hat{t}$ and $+\hat{t}$.

- The adiabatic evolution restarts at $+\hat{t}$, corresponding to $-\hat{\epsilon}$, when the ground state previously frozen suddenly becomes an initial excited state in the last step of evolution.

Thus, we see that in this approximation, when we cross $-\hat{\epsilon}$, the state is equal to the one at $+\hat{\epsilon}$. In the limit of large quench times, the boundaries $\pm\hat{\epsilon}$ are very close to the critical point. Hence, even if at a certain point adiabaticity will end, the expectation value of an operator will be proportional to a power of the diverging $\hat{\xi}$ in the ground state at $\hat{\epsilon}$, following the scaling hypothesis of the renormalization group theory.

For this reason, the scaling of any quantity directly related to the correlation length is predictable. For example, if the target phase admits quasi-particle excitations, it is possible to submit the density of such excitations to the Kibble-Zurek analysis. In particular, the density should scale as

$$n_{\text{ex}} \simeq \hat{\xi}^{-d} \sim \tau^{-\frac{d\nu}{1+\nu z}} \tag{3.30}$$

where d is the number of space dimensions.

3.6 Kibble-Zurek mechanism of the Ising model

In the context sketched in this Chapter, many works have tackled the dynamic behaviour of closed quantum systems. This analysis is interesting especially when a quantum critical point is crossed, implying a phase transition. Nevertheless a wide variety of approaches is possible, both in the dynamics protocol and the considered quantities. For example, the main works focus on quantum quenches [10, 18, 19, 39] or look after correlations [10, 18, 19] in systems. On the other hand, it is possible to investigate the dynamics of entanglement entropy and spectrum [9, 10, 39] and set a quasi-adiabatic protocol [8, 9, 31].

In relation with the previous section, entanglement entropy and spectrum may be suitable to a Kibble-Zurek analysis. If this is the case, we would get an insight on the question about what features are universal in the dynamics of a system following a quantum quench and what are the characteristics of the final state.

The present thesis was inspired by the work by E. Canovi *et al.* published on the Physical Review B [9]. In this paper, the authors studied the time evolution of entanglement entropy and entanglement spectrum in a finite-size model crossing a quantum phase transition. They considered the transverse-field Ising model, with both fast and slow quenches as evolution protocols. In this paragraph we will summarise their results following the original paper quite closely and concentrating only on the paramagnet-to-ferromagnet transition.

3.6.1 The model

The model considered has Hamiltonian

$$\mathcal{H} = -\frac{J}{2}\sum_{j=1}^{L}[\sigma_j^z\sigma_{j+1}^z + h\sigma_j^x] \tag{3.31}$$

where L in the size of the system, which also has periodic boundary conditions. σ_α are the usual Pauli matrices and $h = h(t)$ is a time-dependent magnetic field.

The model shows one quantum critical point at $h = 1$, setting the boundary between two phases:

- A paramagnetic phase for $h \geq 1$;

- A ferromagnetic phase for $0 \leq h < 1$.

The negative part of the phase diagram is exactly specular to the positive one, due to the $\mathbb{Z}_2$ symmetry characteristic of the Ising model. The Hamiltonian is made time-dependent by letting the magnetic field vary as

$$h(t) = h_i + \text{sgn}(h_f - h_i)\frac{t}{\tau} \tag{3.32}$$

where τ is the quench time and $t \in [0, t_f]$, with $t_f = |h_f - h_i|\tau$. In the paper $\hbar = J = 1$, so that time and energy are measured in unit of J. Different values of τ determine different regimes of the model, as we will see in the next paragraph.

In order to study the initial structure of the entanglement spectrum, it is useful to recall the ground state in the paramagnetic region for $h_i \to \infty$ (i.e., for $t = 0$). The lowest energy state is

$$|0\rangle \equiv \prod_{j=1}^{L} |\rightarrow\rangle_j \tag{3.33}$$

where $|\rightarrow\rangle_j$ and $|\leftarrow\rangle_j$ denote the state with spin x-projection $\pm\hbar/2$, respectively. If $h_i \gg 1$, at first order of perturbation, the ground state is given by

$$|GS\rangle = N\left[|0\rangle + \frac{1}{4h}\sum_{j=1}^{L}|j, j+1\rangle\right] \tag{3.34}$$

with

$$|j, j+1\rangle \equiv |\leftarrow\rangle_j |\leftarrow\rangle_{j+1} \prod_{\substack{k=1 \\ k\neq j,j+1}}^{L} |\rightarrow\rangle_k \,, \tag{3.35}$$

i.e. a state with two spin flips at sites j and $j+1$. $N \equiv (1 + \frac{L}{16h^2})$ is the normalisation coefficient.

The bipartition chosen in the paper is always the half-chain $A = \{1, \ldots, L/2\}$. The relative reduced density matrix takes the form

$$\rho_A = \begin{pmatrix} |0\rangle_A, & |2p\rangle_A, & |1\rangle_A, & |L/2\rangle_A \end{pmatrix} \mathbb{R}_A \begin{pmatrix} {}_A\langle 0| \\ {}_A\langle 2p| \\ {}_A\langle 1| \\ {}_A\langle L/2| \end{pmatrix} \tag{3.36}$$

where four different states of the system are considered:

- $|0\rangle_A$, the paramagnetic state relative to subsystem A, arising when the couple of flipped spins of Eq. (3.35) is contained in subsystem B;
- $|2p\rangle_A \equiv \left(\frac{L}{2}-1\right)^{-\frac{1}{2}} \sum_{j=1}^{\frac{L}{2}-1} |j, j+1\rangle$, when the two spins of (3.35) are both contained in A;
- $|1\rangle_A \equiv |\leftarrow\rangle_1 \prod_{j=2}^{\frac{L}{2}} |\rightarrow\rangle_j$;
- $|L\rangle_A \equiv |\leftarrow\rangle_{L/2} \prod_{j=2}^{\frac{L}{2}-1} |\rightarrow\rangle_j$.

In the last two states the couple of spins is separated by the boundary between subsystems. For this reason, it is clear that the latter states are degenerate in energy. We have also

$$\mathbb{R}_A \equiv N^2 \begin{pmatrix} 1+\frac{\frac{L}{2}-1}{16h^2} & \frac{\sqrt{\frac{L}{2}-1}}{4h} & 0 & 0 \\ \frac{\sqrt{\frac{L}{2}-1}}{4h} & \frac{\frac{L}{2}-1}{16h^2} & 0 & 0 \\ 0 & 0 & \frac{1}{16h^2} & 0 \\ 0 & 0 & 0 & \frac{1}{16h^2} \end{pmatrix}, \tag{3.37}$$

showing that $|1\rangle_A$ and $|L/2\rangle_A$ are true eigenstates of ρ_A. On the contrary, for large enough h the remaining two eigenstates are superpositions of $|0\rangle_A$ and $|2p\rangle_A$, one with dominating paramagnet while the other with dominating $|2p\rangle_A$.

A numerical analysis showed that just the first four eigenvalues contribute to the entanglement dynamics of the system. In Figure 3.3 the sum of these four eigenvalues is shown, displaying a partial weight

$$W_4(t) = \sum_{n=1}^{4} \lambda_n(t) \gtrsim 0.97 \tag{3.38}$$

for every quench regime. Therefore, in the paper only these four eigenvalues of the reduced density matrix ρ_A are considered and the relative entanglement entropy is calculated as

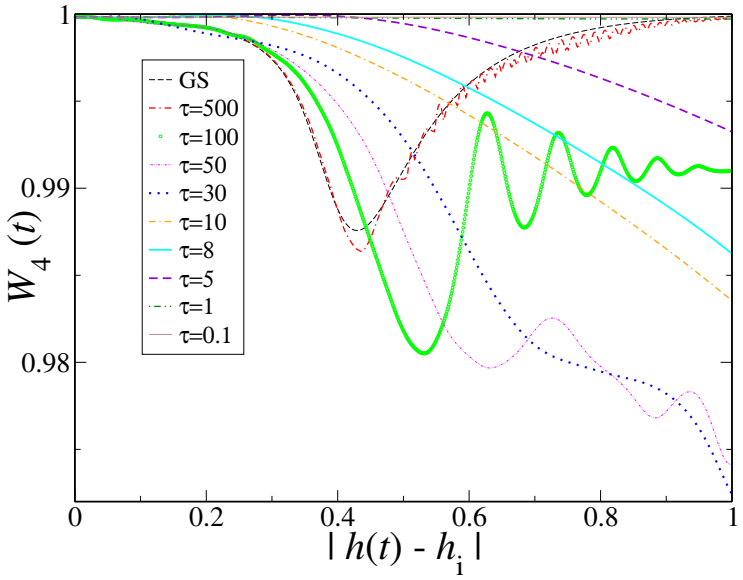

Figure 3.3: Sum of the first four eigenvalues of the reduced density matrix W_4 (as in Eq. 3.38) for $L = 50$, $h_i = 1.4$, $h_f = 0.4$ and different values of τ. Reprint with permission of [9].

$$\tilde{S}(t) = -\sum_{n=1}^{4} \lambda_n(t) \log_2 \lambda_n(t). \tag{3.39}$$

Looking at the response of the system to different quench times τ, three regimes can be individuated: the adiabatic and the sudden ones, along with an intermediate situation in which we have different behaviours depending on the quench time. In the next three paragraphs we will sketch the results.

3.6.2 Adiabatic and sudden quenches

When τ becomes large, the behaviour is quasi-adiabatic: the system follows the static solution related to the ground state of the system for each value of $h(t)$. While in the thermodynamic limit a quantum critical point has a zero gap, at finite size it remains always non-zero, however small. In fact, the real adiabatic limit can be reached only for $\tau \to \infty$. Anyway, it is possible to reach the quasi-adiabatic limit, provided that τ is large enough. This behaviour is shown in the curve for $\tau = 500$ in Figure 3.4 and Figure 3.5(a). The dynamics of the spectrum, whose four eigenvalues become degenerated and stabilise on two self-avoiding values, reflects the $\mathbb{Z}_2$ symmetry of the system.

In the opposite situation, for sudden quenches, the system cannot follow the abrupt changes induced on the Hamiltonian. The evolution is then essentially frozen, independently from the size of the system: curve $\tau = 0.1$ in Figure 3.4

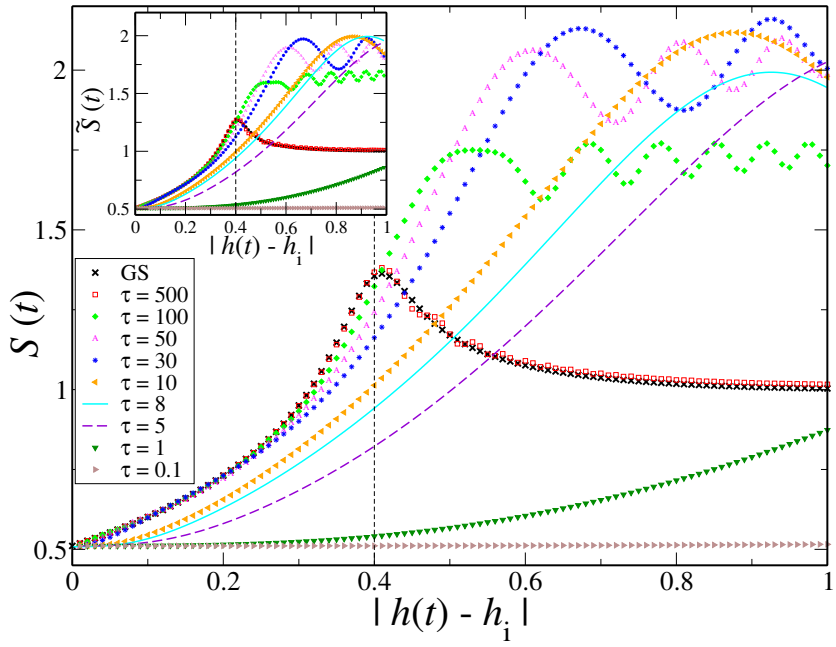

Figure 3.4: Dynamics of the entanglement entropy for $L = 50$, $h_i = 1.4$, $h_f = 0.4$. In the main $S(t)$ is plotted for different values of τ (dashed verical line: location of the critical point). In the inset: $\tilde{S}(t)$ as defined in Eq. 3.39 for the same values of τ as in the main panel. Reprint with permission of [9].

and panel (b) of Figure 3.5 display an entanglement entropy and spectrum not evolving at all.

3.6.3 Fast sweeps

Between these two limits, there is an intermediate region consisting in quench times between 1 and 100. Considering fast rampings with $\tau = 1 \div 30$ first, the authors divide this range in two regimes.

In the first one, they concentrate on quench times $\tau \sim 1$. The entanglement entropy grows linearly in the region near the critical point, as shown by curves with $\tau = 1$ and 5 in the main panel of Figure 3.4. This behaviour was related to the conformal field theory, predicting a linear grow of the entanglement entropy in sudden quenches with a slope related to the central charge [7]. On the other hand, in the entanglement spectrum (shown in Figure 3.5(c)) the first eigenvalue decreases, while the remaining three increase. This homogenisation of eigenvalues causes the linear increase of the von Neumann entropy. For this range of quench times, the degeneracy between second and third eigenvalues is not broken.

As for the second regime with $\tau \sim 10 \div 30$, the entanglement entropy after

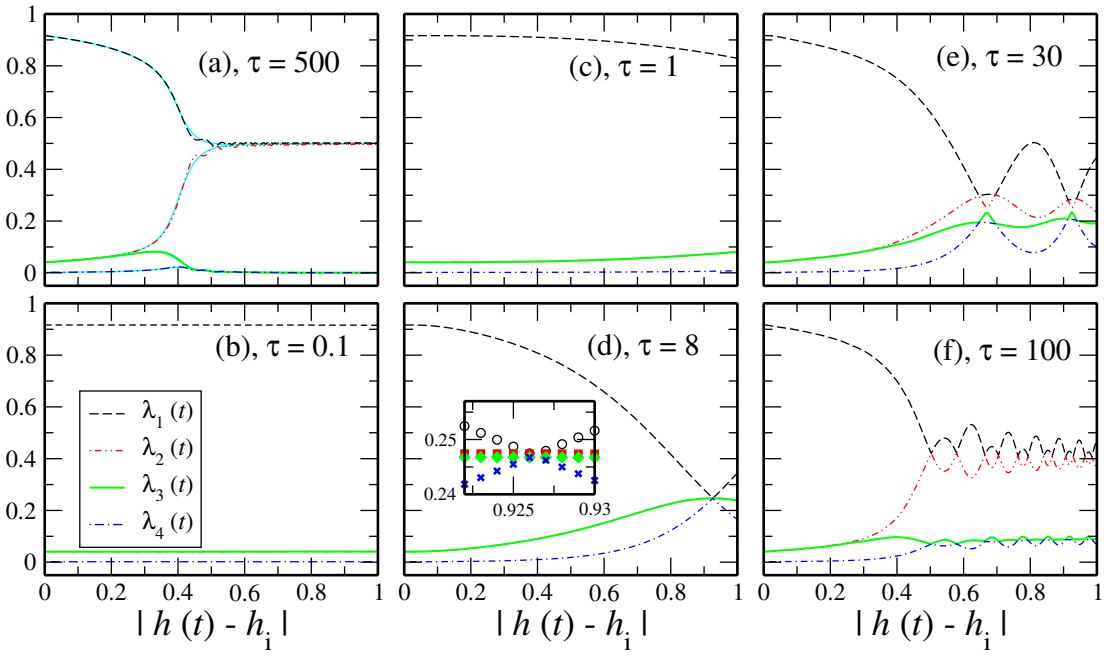

Figure 3.5: Dynamics of the entanglement spectrum for $L = 50$, $h_i = 1.4$ and $h_f = 0.4$. Black dashed, red dot-dot-dashed, green solid and blue dash-dotted lines correspond to the dynamical eigenvalues $|0\rangle_A$, $|1\rangle_A$, $|L/2\rangle_A$ and $|2p\rangle_A$ of the reduced density matrix of the half chain, respectively. Different panels refer to (a): $\tau = 500$; (b): $\tau = 0.1$; (c): $\tau = 1$; (d): $\tau = 8$; (e): $\tau = 30$; (f): $\tau = 100$. In panels (b), (c) and (d) red and green lines overlay. The cyan lines in panel (a) show the ground-state values of the first four eigenvalues. The inset in panel (d) is a zoom of the crossing point. Reprint with permission of [9].

a linear growth ends in an oscillatory region with variable frequencies (see, e.g., curves with $\tau = 8$, 10 and 30 in Figure 3.4). This happens because, after crossing the quantum critical point, the system ends in a superposition of excited states in which the entanglement entropy varies between maxima and minima. The oscillating frequency scales approximately as the energy gap. In the entanglement spectrum, the further decrease of the first eigenvalue and growth of the remaining ones results in a crossing of the four at the same point (as shown in panel (d) of Figure 3.5). This crossing happens periodically in the spectrum after the critical point and is associated to the maxima of entanglement entropy. The crossing point tends to the critical point with good precision for $\tau \to \infty$: this means that oscillations have always the same physical meaning and the displacement of the first crossing point depends on the finite size effects.

3.6.4 Slow sweeps

The slower rampings happen for $\tau \gtrsim 30$. The entanglement entropy (curves $\tau = 50$ and $\tau = 100$ in Figure 3.4) first evolves in the same manner of the static one. Anyway, at a certain value of the sweep (nearer to the critical point with respect to faster rampings) it begins to oscillate with a frequency inversely decreasing with the quench time. This characterise the approach to the adiabatic limit. On the other hand, panels (e) and (f) in Figure 3.5 show the dynamics of the entanglement spectrum in this regime. The second and third eigenvalues cease to be degenerate, while the first and fourth undergo more and more avoided crossings. In panel (f) the situation resembles the quasi-adiabatic one, with crossing between the first and second, third and fourth eigenvalues. However, crossing between the couples happens at the same time and is coincident with the maxima in the entanglement entropy.

3.6.5 Kibble-Zurek analysis

In section 3.5 we described the Kibble-Zurek mechanism and its application in many-body problems. In the paper in question, the authors carry out a Kibble-Zurek analysis of entanglement entropy and Schmidt gap (i.e., the difference between the two highest eigenvalues of the reduced density matrix). We shall concentrate on the former only. As previously seen, any quantity directly dependent on the correlation length can be related to the KZM. The scaling of correlation length with a linear quench of inverse velocity τ is displayed in Equation 3.29. At the same time, as sketched in section 3.3, Calabrese and Cardy showed [7] that entanglement entropy, near to a critical point and for an infinite system, scales as

$$S = \frac{c}{6} \log_2 \xi + \text{const.} \tag{3.40}$$

Thus, using equations 3.29 and 3.40 the entanglement entropy is predicted to scale as

$$S = \frac{c\nu}{6(1+\nu z)} \log_2 \tau + \text{const.} \tag{3.41}$$

where the coefficient of the logarithm in the Ising case for an infinite system is $1/24$, since $\nu = z = 1$ and $c = 1$. The results obtained are plotted in Figure 3.6, as well as the Kibble-Zurek prediction.

The simulation worked with a finite system, so finite-size deviations were expected. Indeed finite-size corrections are manifestly important, as the Kibble-Zurek behaviour clearly breaks down lowering L. Moreover, because of its finite size, the subsystem A has two boundaries: therefore, in Equation 3.41 the loga-

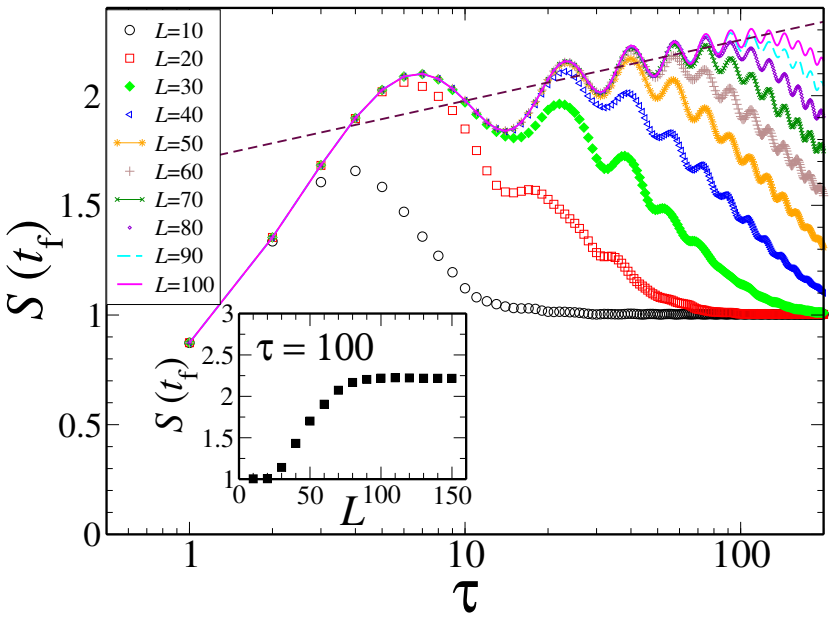

Figure 3.6: In the main panel the entanglement entropy at the final instant of the evolution for $\tau \in [1, 200]$ at different system sizes ($L = 10 \div 100$, from bottom to top) is shown. Dashed maroon line: $y = \frac{1}{12} \log_2 x + \text{const}$. Inset: entanglement entropy at the final instant of the evolution for $\tau = 100$ as a function of the system size L. Reprint with permission of [9].

rithmic coefficient is doubled [6]. It is also clear that the logarithmic behaviour is superimposed to an oscillating one, that reflects the nature of the entanglement entropy. Additionally, for small values of τ the different curves overlay: as the quench time grows, the coincidence is lost depending on the size of the system. The overlap is observed for quench times which correspond to the thermodynamic limit regarding the different system sizes: the smaller is the system, the faster the KZ behaviour breaks down. Finally, the quench times relative to the passage from fast to slow regime, i.e. the end of the crossing between the first and fourth eigenvalues, correspond to the breakdown of the KZM. This coincides with the failure of the thermodynamic-limit description of the system.

The aim of this thesis is to investigate the properties of entanglement entropy and spectrum of the XXZ model from a dynamic point of view. In particular, we will focus on the critical region $-1 < \Delta < 1$ and on the critical point at its boundary, i.e. $\Delta = 1$. We will investigate whether it is possibile to describe the dynamics of the model by means of the Kibble-Zurek mechanism, consistently with the analysis developed in [9], where results where achieved on the Ising model. This task is challenging for several reasons. First, while XXZ model is integrable as well as the Ising model, anyway they belong to different symmetry groups. The Ising model has a $\mathbb{Z}_2$ symmetry, while in the XXZ we have a

SU(2) at the critical points and U(1) = O(2) when $\Delta \neq \pm 1$. Hence, we should expect some different behaviour both in entanglement entropy and entanglement spectrum. Moreover, in the XXZ model the entire region between the QCP is critical, i.e. gapless, and adjoins with two completely different phases. Hence, a dynamic insight in this phase is extremely interesting.

Chapter 4

Density-Matrix Renormalization Group

4.1 DMRG

In the context of many-body problems, one of the crucial aspects limiting our knowledge of systems made of particle ensembles is represented by their exponentially-growing Hilbert-space dimensionality. Just to exemplify, let's think of a one-dimensional 1/2-spin chain whose possible single-site states are $|\uparrow\rangle$ and $|\downarrow\rangle$: the total dimension of the related Hilbert space is 2^L, depending on the length L of the chain. It is evident how rapidly can the number of degrees of freedom grow and how difficult it can become the diagonalisation of related matrices. Due to the size of the Hilbert space, most times it is impossible to find exact solutions and a numerical approach, essentially approximating the description of the system as well as capturing its core physics, is needed. The method called DMRG provides a controlled elimination of the unimportant degrees of freedom, keeping the ones necessary to exahustively describe the system.

DMRG is the acronym of Density-Matrix Renormalization Group: it has been developed by S. White in 1992 [40] and since then has been addressed as the most performing technique of numerical simulation to describe low-energy physics of one-dimensional strongly correlated quantum systems.

Over the years several methods to reduce the Hilbert space in many-body problems have been improved, each one with its particular criterion of choice for the best states (for an overview see [20, 30, 37, 33]). The general idea lying beneath renormalization groups is to keep a certain number m of states sufficiently describing a system Hamiltonian. This task is usually accomplished first considering small blocks in order to diagonalise their matrices in an easier

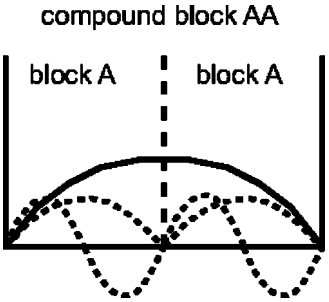

Figure 4.1: Problem of a single particle in a box in the continuum limit. Dashed lines: lowest-lying eigenstates of block A. Solid line: lowest-lying eigenstate of block AA

way and then retaining the corresponding m lowest energy eigenvectors. These states then constitute a starting point for the construction of bigger systems, just as if they were an *ansatz*. This happens for example in the *real-space normalization*, the real precursor of DMRG developed by Wilson [42]. In this procedure, an Hamiltonian $\mathcal{H}_A$ describes a block of length ℓ in a M-dimensional Hilbert space. This block, along with a similar one, forms a unique superblock AA of length 2ℓ with Hamiltonian $\mathcal{H}_{AA}$. A diagonalisation of this Hamiltonian is performed to find its lowest m eigenvalues. Then the Hamiltonian is projected on the space spanned by this truncated m-dimensional basis, resulting in $\hat{\mathcal{H}}_{AA}$. These steps are repeated taking $\hat{\mathcal{H}}_{AA}$ as $\mathcal{H}_A$. As we see, the ground states of the single blocks form the basis to build the wave functions describing bigger blocks. Anyway, while this approach yielded acceptable results for a certain category of physical systems - such as in the Kondo problem [42] - it happened to fail when applied to quantum lattice problems. S. White and R. M. Noack pointed out [41] that the problem with this method consists entirely in the isolation of the block from the environement, i.e. in its treatment of boundary conditions.

As we can see in Figure 4.1, the solution of the blocks considered individually will never result in the ground state of the superblock, for the product states of the A blocks always have a node in the AA block center. However, this is exactly the point where the real ground state of the superblock would reach its maximum amplitude. This qualitative consideration allows to understand the crucial problem of this renormalization technique: if the blocks are considered as isolated, the boundary conditions lead to solutions good enough for the single block but insufficient for the description of an interacting system. Hence, the key is to consider always the block along with an environment, to mimick the interaction with the surroundings.

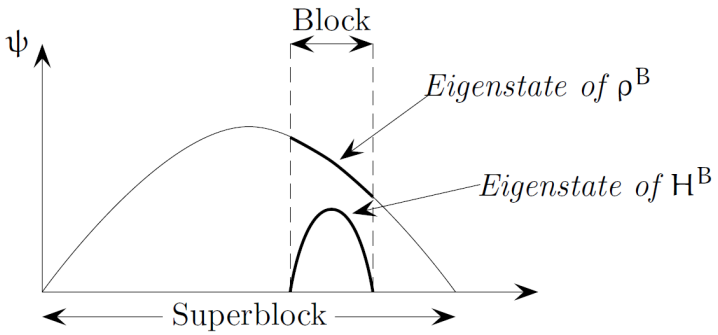

Figure 4.2: Difference between an eigenstate chosen using density matrix or Hamiltonian: the former fits perfectly the target state, while the last does not due to boundary conditions

4.1.1 Density-matrix description

The use of density matrices comes up with the question of what states of the block will best describe the system as a whole, i.e. retain information about the links with the environement. The states we have to choose are obviously the most probable ones where we can find the block. What is not obvious is that these states may not be associated at all with the lowest-energy ones of the isolated block, as it is qualitatively depicted in Figure 4.2. Density matrices fulfill this precise task, as they are a complete description of quantum physical systems in pure as well as mixed states (see Section 3.2 along with its references). Therefore, they can carry the information about the entanglement of the block with the environement. We now rapidely review the basic physical description of a partitioned system using density matrices.

Let the ground state of the superblock be represented by $|\psi_0\rangle$. As we recalled in Section 3.2, a partition of the system will generally result in a mixed entangled state. Denoting the complete basis for the block with $|\alpha_i\rangle$ and the one for the environment with $|\beta_i\rangle$, we can represent the state as

$$|\psi_0\rangle = \sum_{i,j} \Psi_{i,j} |\alpha_i\rangle |\beta_j\rangle . \tag{4.1}$$

If we consider an operator $\mathcal{A}^B$ acting only on the block, we have

$$\begin{aligned}\left\langle \mathcal{A}^B \right\rangle_{\psi_0} &= \sum_{i,i',j,j'} \Psi^*_{i,j}\Psi_{i',j'} \left\langle \beta_j \right| \otimes \left\langle \alpha_i \right| \mathcal{A}^B \left| \alpha_{i'} \right\rangle \otimes \left| \beta_{j'} \right\rangle \\ &= \sum_{i,i'} \sum_{j} \Psi^*_{i,j}\Psi_{i',j} \left\langle \alpha_i \right| \mathcal{A}^B \left| \alpha_{i'} \right\rangle \end{aligned} \tag{4.2}$$

since $\langle \beta_j \,|\, \beta_{j'} \rangle = \delta_{jj'}$. The block density matrix is defined as

$$\left\langle \alpha_{i'} \right| \rho^B \left| \alpha_i \right\rangle = \sum_j \Psi^*_{i,j}\Psi_{i',j} \tag{4.3}$$

where the ennvironement degrees of freedom have been traced out. As a consequence, we have

$$\left\langle \mathcal{A}^B \right\rangle_{\psi_0} = \sum_{i,i'} \left\langle \alpha_i \right| \mathcal{A} \left| \alpha_{i'} \right\rangle \left\langle \alpha_{i'} \right| \rho^B \left| \alpha_i \right\rangle = \mathrm{tr}(\rho^B \mathcal{A}) \tag{4.4}$$

Thus, the DMRG chooses for each block the set of states which are the best possible to describe the block itself as well as to construct the superblock. It finds an eigenstate of the superblock (called *target state*), then traces out the degrees of freedom belonging to the environement. The remaining reduced density matrix is diagonalised: its eigenvalues represent the probabilities of the corresponding eigenvectors.

At this point the real approximation takes place, because the algorithm will retain only m of these eigenvalues. This step is called *truncation*: in the choice of the number of retained states lies all the reliability of the algorithm. The quantity used to estimate this precision is the discarded weight. It is defined as the sum of the discarded eigenvalues, i.e.

$$\epsilon_{\mathrm{disc}} = \sum_{i=m}^{N} \lambda_i \tag{4.5}$$

being λ_i the eigenvalues and N the dimension of the system's Hilbert space. The smaller is ϵ_{disc}, the bigger the amount of information retained for the next step of the DMRG.

4.1.2 The algorithms

In order to complete this qualitative description of DMRG, the problem of adding degrees of freedom to the system - i.e., let the system grow - is yet to be addressed. The construction of the system is made adding a site for each loop, to minimize the number of degrees of freedom to process at every step. Moreover, the choice of the environement block determines different procedures in DMRG.

In general, from this point of view, the DMRG algorithms divide in two classes that are often used in combination for a reason that will be explained in a moment. These classes are the *infinite system algorithm* and the *finite system algorithm*.

In the *infinite system algorithm* the enviroment is a reflection of the system block, including the added site. Therefore, at each step the superblock grows of two sites, one for the block and the corresponding one for the environement. This algorithm is usually employed to build a system of a particular size starting from small blocks, in order to have a good initial approximation to improve with the finite size algorithm. The steps composing a single loop for this procedure are the following:

1. Formation of a superblock made of L sites and small enough to allow exact diagonalisation, its Hamiltonian being $\mathcal{H}_L^{\text{super}}$.

2. Diagonalisation of $\mathcal{H}_L^{\text{super}}$, obtaining its ground state eigenvalue and corresponding eigenvector ψ using the Lanczos or Davidson algorithm.

3. With the latter state, formation of the reduced system matrix $\rho_{i,i'}$ for the current block using Eq. 4.3. In this situation index i corresponds to the block, whose size will be $\ell = L/2 - 1$, while index j corresponds to the environement, with the same size ℓ'. Between these blocks, there are two single sites.

4. Diagonalisation of $\rho_{i,i'}$ to obtain its eigenvectors. Only m of these, with bigger eigenvalues, will be retained.

5. Construction of the Hamiltonian $\bar{\mathcal{H}}_{\ell+1}$ for the new system block (made of the old block plus the single site) and calculation of the needed observables. For the formation of the effective Hamiltonian, a change of basis to the new set of block eigenstates is needed. Denoting with $\mathbf{H}_{\ell+1}$ the Hamiltonian matrix of the system and with $\mathbf{A}_{\ell+1}$ a generic operator matrix, we have

$$\bar{\mathbf{H}}_l = \mathbf{O}_L^\dagger \mathbf{H}_{\ell+1} \mathbf{O}_L \tag{4.6}$$

   where $\mathbf{O}_L$ is an $m \times l$ whose columns contain the m eigenvectors of $\rho_{i,i'}$, and

$$\bar{\mathbf{A}}_{\ell+1} = \mathbf{O}_L^\dagger \mathbf{A}_{\ell+1} \mathbf{O}_L. \tag{4.7}$$

   The same is done for the environement.

6. Formation of a new superblock of size $L+2$ using $\bar{\mathcal{H}}_{\ell+1}^{\text{block}}$, two single sites and $\bar{\mathcal{H}}_{\ell'+1}^{\text{env}}$.

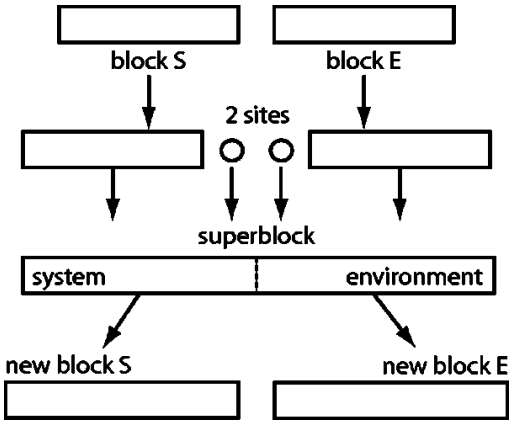

Figure 4.3: Infinite system algorithm

7. Restart from step 2 replacing $\mathcal{H}_L^{\text{super}}$ with $\bar{\mathcal{H}}_{L+2}^{\text{super}}$.

The infinite system method targets a different wave function at each step because of the growth of the lattice site. This may lead to a lack of convergence with m if the wave function changes qualitatively between the steps (for example, due to the injection of particles during system growth in electronic systems). The *finite system algorithm* manages to solve this sort of problems. The general idea behind this procedure is to stop the infinite system algorithm at some L kept fixed: in the following steps the growth of a block corresponds to the shrinkage of the other block. The finite system procedure can be sketched as follows:

1. Completion of the infinite system algorithm until the superblock reaches size L, storing the Hamiltonian $\bar{\mathcal{H}}_\ell$ and the operators connecting the blocks at each step.

2. Formation of the reduced density matrix, diagonalisation to obtain its eigenvectors, choice of the m lowest ones. Then, construction of the new Hamiltonian $\bar{\mathcal{H}}_{\ell+1}^{\text{block}}$ and storage. At this point, the size of the block and of the environement are different.

3. Buildup of a superblock of size L using $\bar{\mathcal{H}}_{\ell+1}^{\text{block}}$, two single sites and $\bar{\mathcal{H}}_{\ell'-1}^{\text{env}}$. We now have $\ell' = L - \ell - 2$

4. Repetition of steps 2-3 until environement block reaches some minimum size (let us suppose it is $\ell' = 1$) and becomes exact: thus, when $\ell = L - 3$, the left-to-right phase of the algorithm is completed.

5. Repetition of all the procedure reversing the roles of $\bar{\mathcal{H}}_\ell^{\text{block}}$ and $\bar{\mathcal{H}}_{\ell'}^{\text{env}}$. Thus, the growing block is now the right one, while the left block shrinks:

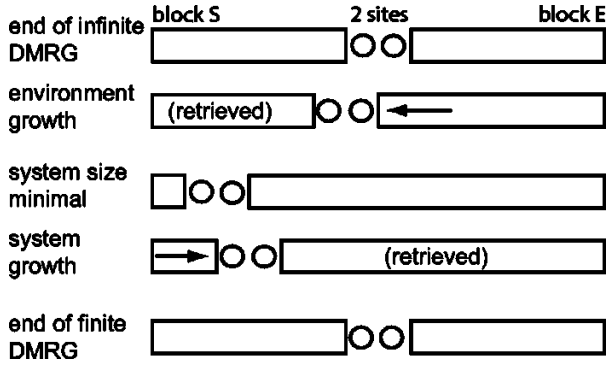

Figure 4.4: Finite system algorithm

the new Hamiltonian is $\bar{\mathcal{H}}^{\text{env}}_{\ell'+1}$.

6. Formation of a superblock using the previously stored $\bar{\mathcal{H}}^{\text{block}}_{\ell-1}$, two single sites and $\bar{\mathcal{H}}^{\text{env}}_{\ell'+1}$.

7. Repetition of steps 2-3 until $\ell = 1$. This is the right-to-left phase.

When the starting point is reached, a full *sweep* has been completed. Usually a few sweeps ensure convergence.

4.1.3 tDMRG

All the previous sections dealed with equilibrium situations, and the kind of DMRG described to obtain the related physical properties may be properly addressed as 'static'. Anyway, time-dependent phenomena are involved in a lot of physical problems concerning strongly correlated quantum systems. Now the basis of (time-dependent) tDMRG will be briefly revised [37].

Time evolution in quantum mechanics is governed by the time-dependent Schrödinger equation

$$i\hbar\frac{\partial}{\partial t}\left|\Psi(t)\right\rangle = \mathcal{H}\left|\Psi(t)\right\rangle \tag{4.8}$$

whose formal solution is

$$\left|\psi(t)\right\rangle = e^{-i\mathcal{H}t}\left|\psi(0)\right\rangle . \tag{4.9}$$

In our thesis - and quite tipically - we are interested in the time evolution of the system after a perturbation $V_{\text{eff}}(t)$ is switched on at $t = 0$, so that the effective Hamiltonian becomes

$$\mathcal{H}_{\text{eff}}(t) = \mathcal{H}_{\text{eff}}(0) + V_{\text{eff}}(t) \tag{4.10}$$

where $\mathcal{H}_{\text{eff}}(0)$ is the last superblock Hamiltonian approximating $\mathcal{H}(0)$.

In order to calculate the eigenstates of the time evolution it is necessary either to integrate Eq. 4.8 directly or to find a good approximation for the unitary time-evolution operator $\mathcal{U}(t)$. Both approaches have been used, but we will sketch only the one implemented in the code used for this work of thesis.

In the direct approach, a Runge-Kutta 4^{th}-order integration [35] of the time evolution is carried out. The Runge-Kutta is an iterative method used to approximate the solutions of ordinary differential equations (such as the Schrödinger time-dependent one). Once we know the initial conditions, this method expresses the solution for the following time increment as a series expansion converging to the exact solution until the 4^{th} order – hence the name. Thus, the local error grows as the fifth power of time step.

In addition, the main difficulty in evaluating time evolution using DMRG is that the effective basis determined at the beginning of the time step cannot properly represent the evolved state. In fact, this method is based on the approximation that the states found for a precise time step will also fit the new Hamiltonian describing the evolved system, provided that the time step is small enough to avoid abrupt variations. For this reason, while Runge-Kutta let the wavefunction evolve, the (truncated) Hilbert space, in which these states live, is adapted to follow the new instantaneous Hamiltonian. This is an additional source of error. Moreover, the Runge-Kutta approximation does not preserve unitarity, so on long times the process may become unstable and lose precision.

4.1.4 Implementation

The DMRG used in this work has been primarily implemented by F. Ortolani, professor in the Department of Physics and Astronomy of the University of Bologna. It uses the Lanczos algorithm [26] to provide iterative diagonalisation of the matrix representation of Hamiltonians. This implementation also admits time-dependent simulations, using the algorithm of Runge-Kutta to approximate the unitary time evolution of the described system, as rapidely sketched in the previous section. The code provides the possibility to restrict the analysis to a particular symmetry present in the relative Hamiltonian. For example, in our case, it was possible to choose a sector with defined magnetisation for the states to be sought. Taking advantage of the symmetries of the Hamiltonian can reduce the Hilbert space size [20]. It also allows us to consider a smaller number of states, improve precision and obtain eigenstates with definite quantum numbers.

4.2 Static simulations

In this section we discuss the results of static simulations obtained via DMRG on the XXZ model. This was done in order to identify the proper set-up for the following analysis: indeed, the static solution of XXZ model is already widely known. The Hamiltonian describing the XXZ model is the one outlined in Section 2.2:

$$\mathcal{H} = -J \sum_{i=1}^{N} \{S_i^x S_{i+1}^x + S_i^y S_{i+1}^y + \Delta S_i^z S_{i+1}^z\} - h_0 S_1^z. \tag{4.11}$$

We assume $J = \hbar = 1$, so that energy will be measured in units of J and time in units of J^{-1}. On the first site of the chain we apply a small magnetic field ($h_0 = 0.01$) in order to break the energy degeneracies and distinguish states with same total magnetisation but different configurations. As a matter of fact, since $\mathcal{H}$ commutes with the total spin component $S_z(L)$, the external magnetic field results in an additional energy contribution without affecting the eigenfunctions. In this way the states in each multiplet are energetically ordered and a unique ground state is selected.

In this work we are mainly interested in the time evolution of entanglement entropy, entanglement spectrum and half-chain magnetisation. They all are quantities suitable to characterise the dynamic profile of a quantum system, as shown for the Ising model in Sec. 3.6. Hence, we will describe the most relevant static results first, just to fix a reference sample.

In this thesis we focus on a spin chain of $L = 12$ sites, fixing open boundary conditions. While it surely is a system still affected by size effects, however its dimension is sufficiently high to display a qualitatively universal behaviour, as we checked comparing static results with the ones for $L = 14, 16, 18, 20, 28, 30, 38, 40$ (not shown). Moreover, we choose to remain on this chain dimension both because this is a preliminary work and in order to leave the computation feasible. Indeed, in the static case, we are still able to get exact diagonalisation and consequent exact results. In the context of dynamics, we are mainly concerned with the paramagnetic-to-ferromagnetic transition, corresponding to $\Delta = 1$ in the phase diagram of the model. In fact, this transition is more detectable than the one at $\Delta = -1$, due to its energy gap opening as a power law. Secondly, we are interested in the dynamic ordering across a phase transition, much more easy to describe when passing from a disordered to an ordered phase.

As we mentioned in the previous Section, the DMRG allows to take advantage of the system symmetries and to fix the quantum number we are interested in. In this case, three different sectors for the magnetisation are considered.

1. The first one, with $S_z = 0$ magnetisation, is presented in Fig. 4.5. On top

panel (a), we have the entanglement entropy, calculated using Eq. 3.2: in our work we take as subsystem half the chain, i.e. $\ell = L/2 = 6$. The transition is well marked at $\Delta = 1$, where the entanglement entropy of the ground state reaches a maximum. The half-chain magnetisation allows us to get a further insight on the structure of the ground states of both the paramagnetic and ferromagnetic phases. In the paramagnetic phase the mean magnetisation on every length scale is zero, as shown by the first part of the curve. On the contrary, in the vicinity of the quantum critical point, $S_z(L/2)$ starts to increase, tending then to the value of 3. When the system moves to the ferromagnetic phase, spin alignement is favoured so an order starts to form. At the same time, the DMRG selects only states with null total magnetisation - as can be checked in panel (c) -. The result is that the configuration with the lowest energy satisfying all these requirement is a chain with half spins up and half down. We note that we do have a residual degeneracy, depending on the energetic equivalence whether the first half of the chain is all up or all down (this can be clearly noted in Fig 5.9(b), where the first two level are evidently equally energetic as they show opposite configurations). Setting an initial small magnetic field removes this degeneracy, selecting one of these two possibilities, i.e. the one with the left half of the chain up . In the next we'll always assume such a degeneracy removal.

2. We then move on the sector with maximum possible magnetisation, that is $S_z = 6$, displayed in Fig. 4.6. The results are quite predictable: the half-chain magnetisation (panel (b)) is always the same for every value of the anisotropy parameter, and its value is exactly half the total S_z (panel (c)). There is only one state showing such a configuration, with all spins pointing up: hence, its entanglement entropy is always null and doesn't give us information on the transition. However, this state is clearly the real ground state for the ferromagnetic phase of the model. For its triviality, further analysis will not be performed in this sector.

3. Lastly, we set DMRG in order not to move in a specified sector: we will mark this configuration as 'undetermined sector'. The corresponding results are shown in Fig. 4.7. They exhibit a merge of the previous data: in fact, in this case for every value of Δ the DMRG finds the lowest energy state, no matter which sector it belongs to. Hence, before the critical point we have curves exactly superimposable to the ones of $S_z = 0$ for all quantities. On the other hand, once passed the transition point, the curves closely follow the real ground state of the ferromagnetic region, found in the $S_z^{\max}$ sector.

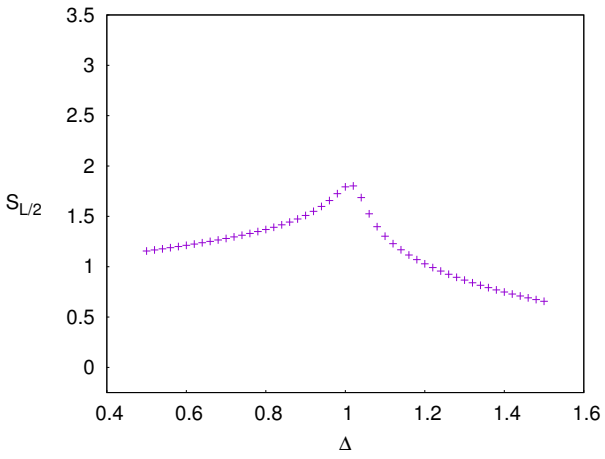

(a) *Entanglement entropy.*

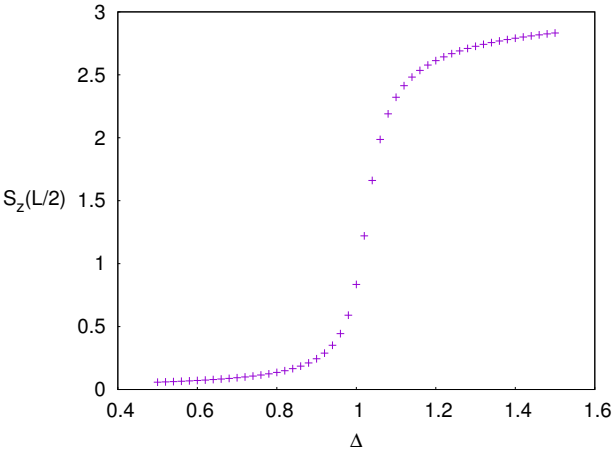

(b) *Half-chain magnetisation.*

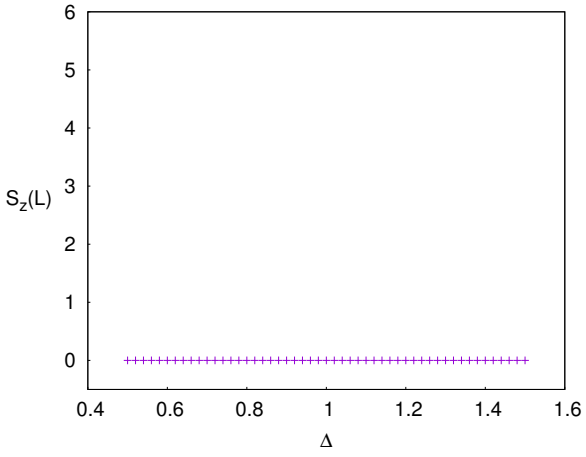

(c) *Total magnetisation.*

Figure 4.5: Static simulations for $L = 12$, within fixed $S_z = 0$ sector.

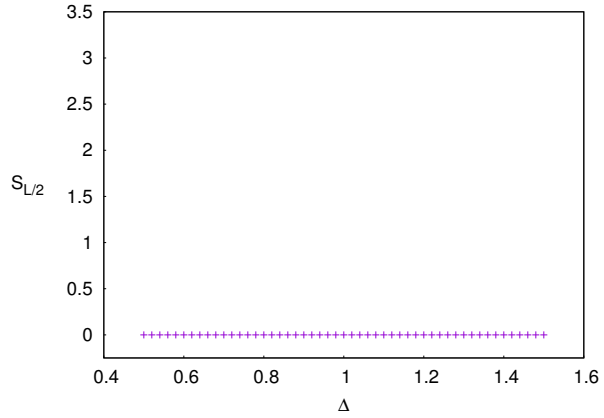

(a) *Entanglement entropy.*

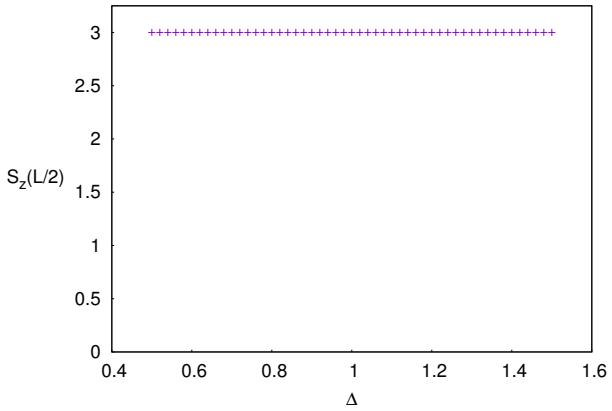

(b) *Half-chain magnetisation.*

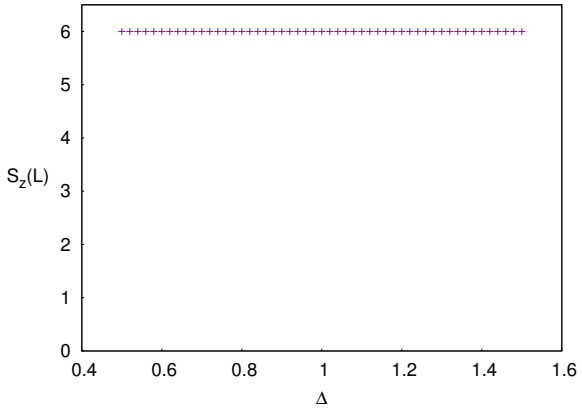

(c) *Total magnetisation.*

Figure 4.6: Static simulations for $L = 12$, within fixed $S_z = 6 \equiv S_z^{\max}$ sector.

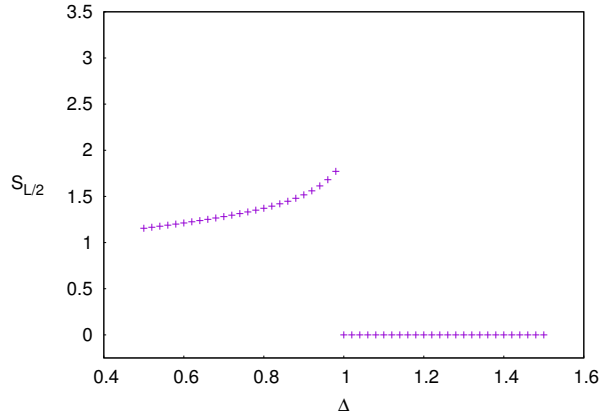

(a) *Entanglement entropy.*

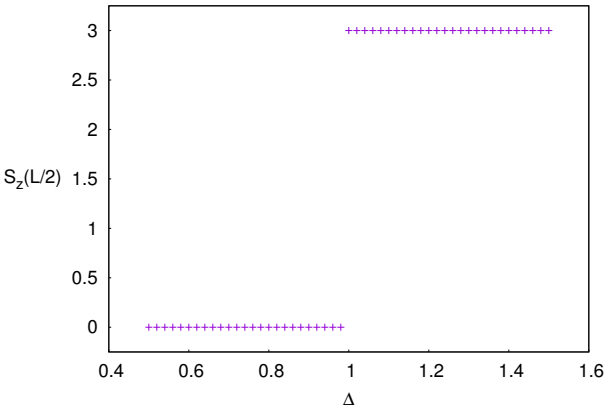

(b) *Half-chain magnetisation.*

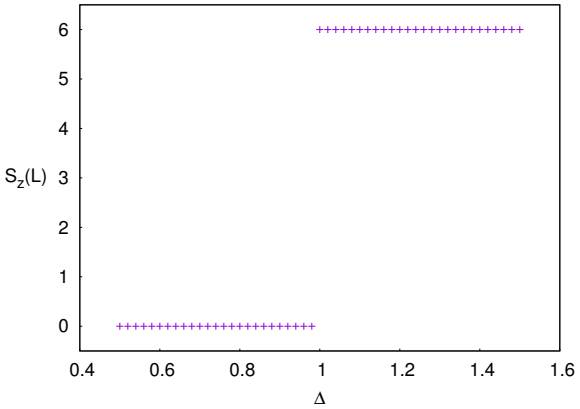

(c) *Total magnetisation.*

Figure 4.7: Static simulations for $L = 12$, within undetermined S_z sector.

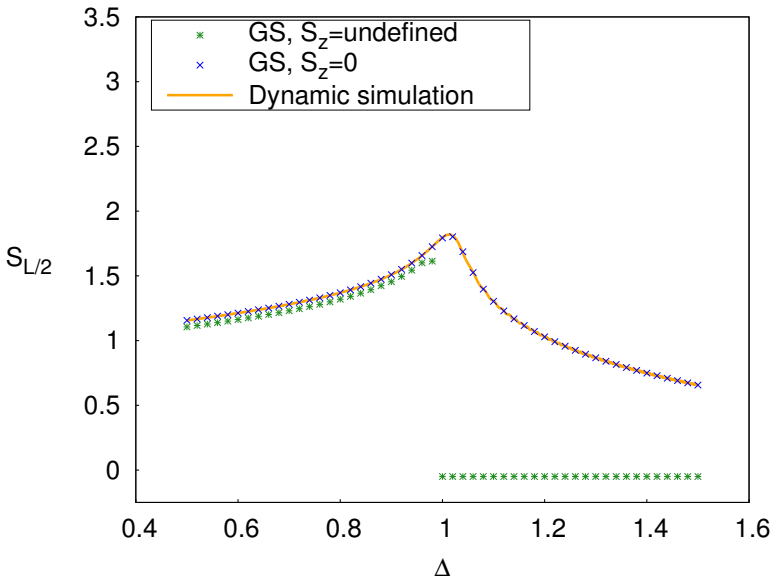

Figure 4.8: Entropy entanglement in static and dynamic simulations for $L = 12$. The static results are displayed both for the sector with fixed magnetisation $S_z = 0$ and for the undetermined sector. The dynamic simulations is performed with adiabatic protocol at $\tau = 4000$.

While this last configuration would be the ideal one for the characterisation of the ground state also for a dynamic simulation moving through different sectors, Figures 4.8 and 4.9 evidently show that the dynamic simulations, though performed with the configuration of 'undetermined sector', strictly follow the curves of $S_z = 0$. So, why would the DMRG not choose the lowest-energy states when reaching the ferromagnetic phase? The reason lies in the Hamiltonian symmetry itself. Just befor starting the real dinamic evolution, the DMRG performs a static simulation to fix the ground state of the system to evolve. Nonetheless, the Hamiltonian commutes with the total magnetisation of the quantum state no matter what the value of Δ is, as mentioned in Sec. 2.1. Thus, once a magnetisation sector has been targeted, the subsequent states will always be sought in there. In our case, starting from the paramagnetic region, whose ground state has $S_z = 0$, for the rest of time evolution the simulation will continue in this specific sector even if we are in a DMRG 'undetermined' configuration. We checked (not shown) that starting from the ferromagnetic point and performing a "Δ-reversed" evolution results in a steady ground state with all spins up in the chain, i.e. the ground state of the ferromagnetic phase, also in the paramagnetic region. For all this reasons we decided to concentrate on the fixed sector $S_z = 0$ in all the rest of the work (so, it will be assumed that we are always dealing with states whose total magnetisation is null).

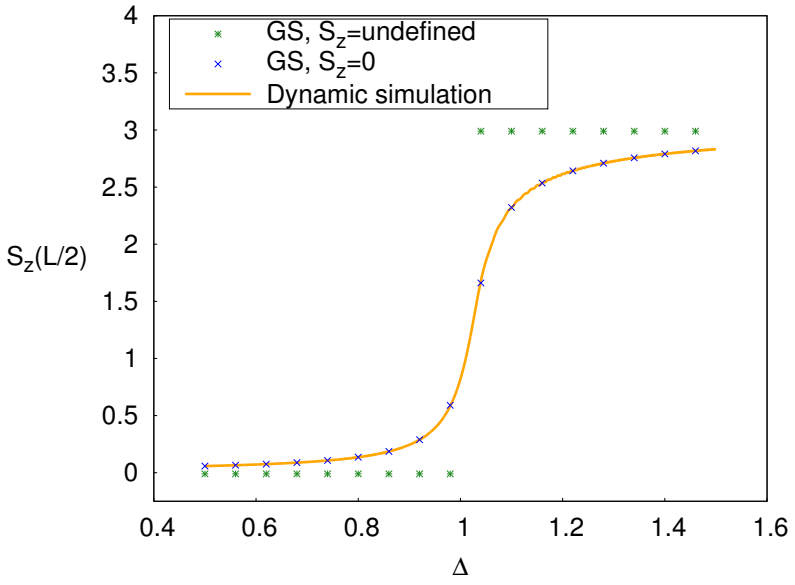

Figure 4.9: Half-chain magnetisation in static and dynamic simulations for $L = 12$. The static results are displayed both for the sectors with fixed magnetisation $S_z = 0$ and for the undetermined sector. The dynamic simulation is performed with adiabatic protocol at $\tau = 4000$.

Chapter 5

Numerical Results

This chapter is entirely devoted to the new dynamical results obtained via tDMRG on the XXZ model. The main parameter to set in the dynamic simulation is τ, i.e. the quench time of the evolution (see Sec. 3.6). As a matter of fact, in our case the quench protocol consists in letting the $\Delta = \Delta(t)$ change linearly in time, from Δ_i to Δ_f:

$$\Delta(t) = \Delta_i + \frac{t}{\tau} \tag{5.1}$$

where $t \in [0, t_f]$, with $t_f = |\Delta_f - \Delta_i|\tau$. As outlined for the Ising model, we expect very different behaviours depending from the value of τ. In addition to the previous quantities, in the dynamic evolution we also study the entanglement spectrum, i.e. the set of eigenvalues $\{\lambda_n\}(t)$ of ρ_A, the density matrix of the ground state of the half-chain subsystem. We always choose the first 6 eigenvalues, corresponding to the eigenvectors that are sufficient to best describe the Hamiltonian: as a validation we checked that, in every regime,

$$W_6(t) = \sum_{i=1}^{6} \lambda_i(t) \approx 1. \tag{5.2}$$

up to an error of 4%.

5.0.1 Dynamic simulations

1. The first regime we consider is the proper quench protocol, i.e. very small values of τ. This situation is illustrated in Fig. 5.1. The dynamics is essentially frozen, and all quantities evolve almost not at all. For the moment, we only note that there is one preminent eigenvalue with nearly the same weight during all protocol. Anyway, towards the end of the evolution it slightly bends down, while the remaining eigenvalues increase:

this causes the faint growth in entanglement entropy.

2. Secondly, we have a wide range of intermediate quench rates which are carachterised by oscillations, varying in amplitude and frequency. An example of these behaviour is displayed in Fig. 5.2 for $\tau = 500$. Here the situation of entanglement spectrum (panel (c)) is far more complicated than the previous one. While the initial distribution is the same as for $\tau = 1$, now the first eigenvalue decisively decreases, and the growth of the remaining ones ends up in a sequence of crossings near the transition point. After $\Delta = 1$, two eigenvalues have a preminent weight and oscillate vigorously with incostant but synchronous frequency. The other eigenvalues fall rapidly to zero.

   It is now interesting to note that such eigenvalue oscillations are strictly related to oscillations both in entanglement entropy and half-chain magnetisation. In Fig. 5.3, vertical lines evidence that the frequency oscillations in the entanglement spectrum determine the pattern in the observables. However, the inconstancy of such oscillations allow only a qualitative analysis in this work.

3. Lastly, we move on to the adibatic regime, corresponding to very large values of τ as in Fig. 5.4. The entanglement spectrum situation of the intermediate regimes reaches its limit: near the quantum critical point the eigenvalues repeatedly cross each other, ending up with two predominant curves. These eigenvalues are now well separated and oscillate with an extremely small amplitude but high frequency. As a result, little oscillation is observable in entanglement entropy and half-chain magnetisation.

It is now necessary to clarify some details of the set-up left uncommented until now.

First of all, concerning the range of the Δ: we move in $0.5 < \Delta < 1.5$. This particular choice of range has been fixed after checking that the main results do not change starting from or arriving to different points, as can be seen in Fig. 5.5. The important information we can extract from this evidence is that the behaviour of the system experiencing the quantum phase transition is mainly depending on the critical point itself, even if this point is the boundary of an entirely critical region (see also [31]). In some way this recalls the adiabatic-impulse-adiabatic approximation described in the context of Kibble-Zurek mechanism in Section 3.5: the behaviour of the system passing a quantum phase transition can all be ascribed to the loss of adiabaticity in the critical point, at least in this case. Hence, no matter the starting point and the end point of evolution, the core physics remains the same and we can choose

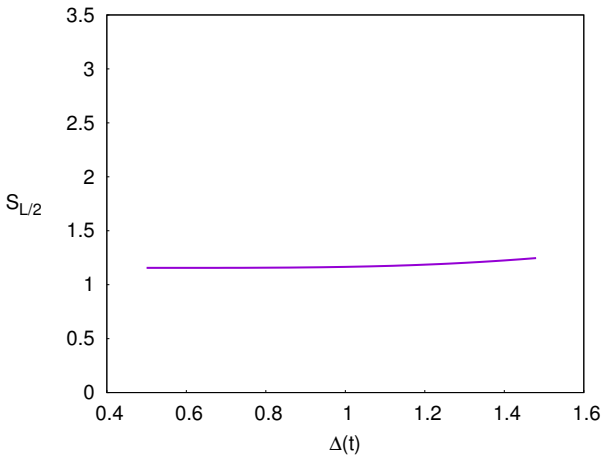

(a) *Entanglement entropy.*

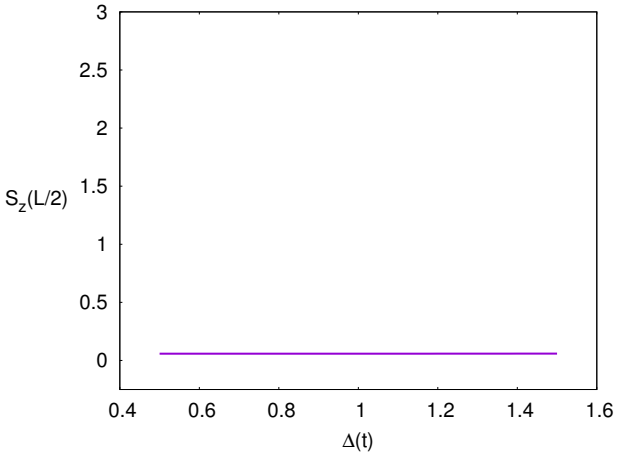

(b) *Half-chain magnetisation.*

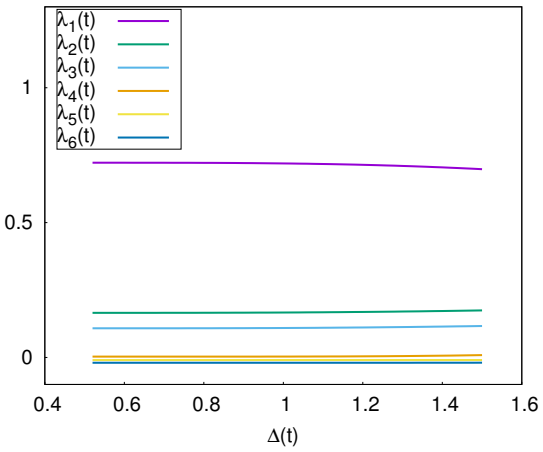

(c) *Entanglement spectrum.*

Figure 5.1: Dynamic simulations for $L = 12$, with quench time $\tau = 1$.

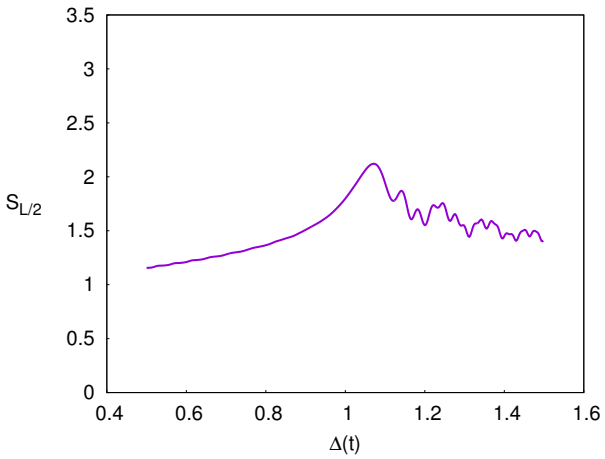

(a) *Entanglement entropy.*

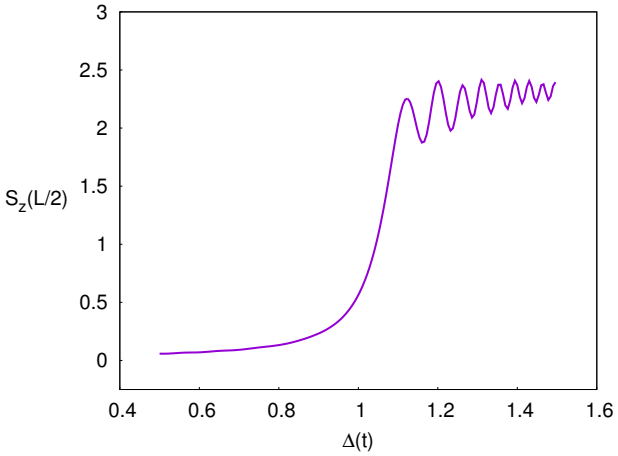

(b) *Half-chain magnetisation.*

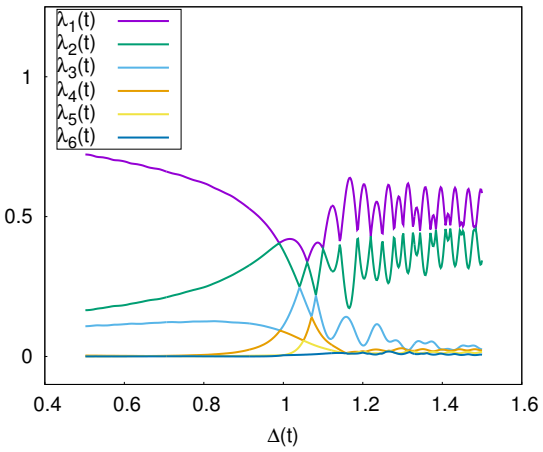

(c) *Entanglement spectrum.*

Figure 5.2: Dynamic simulations for $L = 12$, with quench time $\tau = 500$.

the most convenient set-up.

In addition, we already mentioned that for the purpose of studying ordering in quantum phase transitions, passing from a disordered to an ordered phase is much more suitable to analyisis (for example, looking at the formation of defects or the development of a net magnetisation) than the opposite protocol. Anyway, the dynamic evolution from the ferromagnetic to the paramagnetic region needs a comment. In Fig. 5.6 it is shown an adiabatic evolution from $\Delta = 1.5$ to 0.5. It is evident that, for every quantity, the time-evolution profile is exactly specular to the adiabatic simulations with Δ varying from 0.5 to 1.5, which we report for easier comparison in the right column of the figure. This perfect overlap is observed only in the adiabatic limit. Even though deeper analyses (particularly in the thermodynamic limit) should be carried out in order to confirm such an hypothesis, we may prudently ascribe this effect to the integrability of the considered quantum system. Indeed, quantum integrability in a sense forces the system to access only some states during its evolution. However, when quench times are faster, the states called in the evolution are far less than for high values of τ – for a reason which will soon explained – and the consequent effects are barely visible. Instead, the restricted Hilbert-space structure is recovered in the quasi-adiabatic limit, when the system can access to all the set of states: in this case, the profile of its entanglement entropy, half-chain magnetisation and entanglement spectrum remains the same no matter the direction of the evolution.

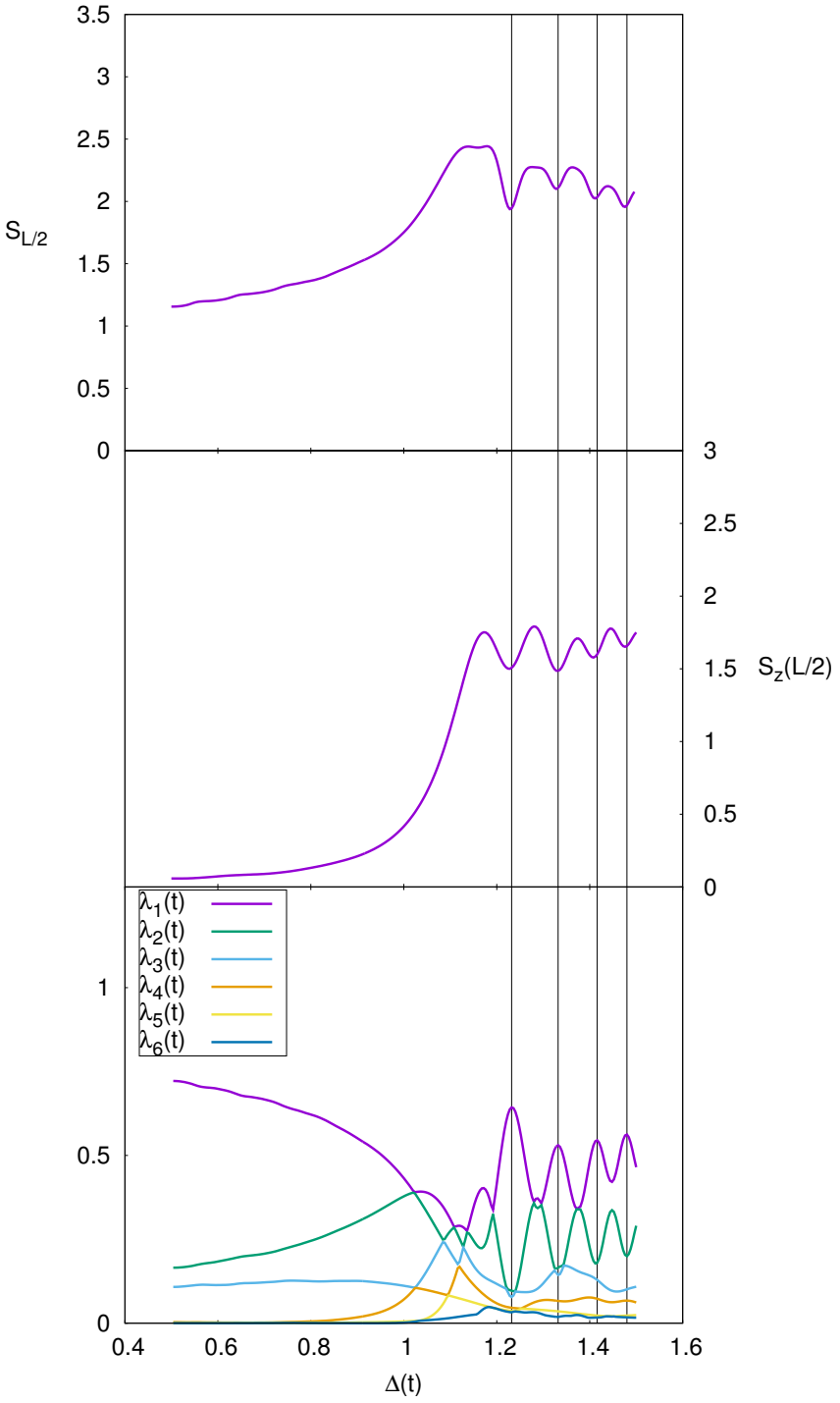

Figure 5.3: Oscillating behaviour of entanglement entropy, half-chain magnetisation and entanglement spectrum for $L = 12$ and $\tau = 250$. Vertical lines highlight correspondences.

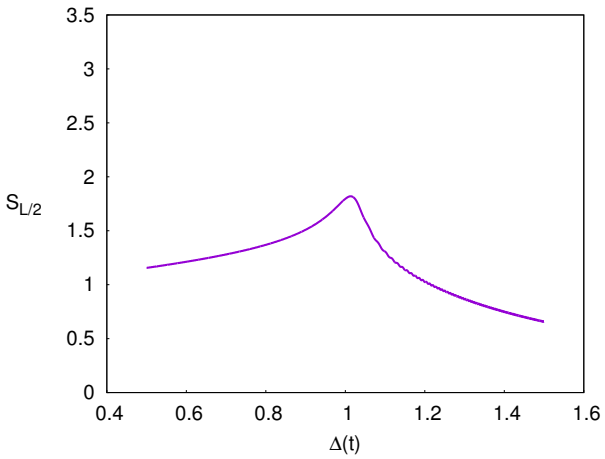

(a) *Entanglement entropy.*

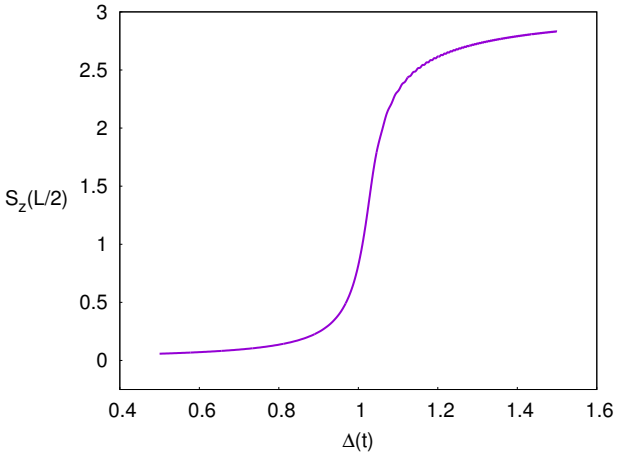

(b) *Half-chain magnetisation.*

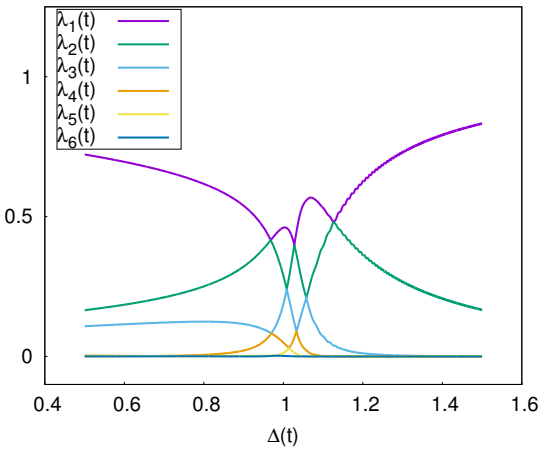

(c) *Entanglement spectrum.*

Figure 5.4: Dynamic simulations for $L = 12$, with quench time $\tau = 4000$.

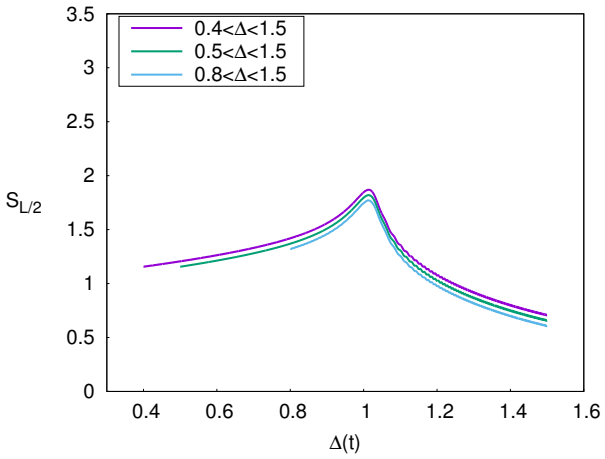

(a) *Entanglement entropy.*

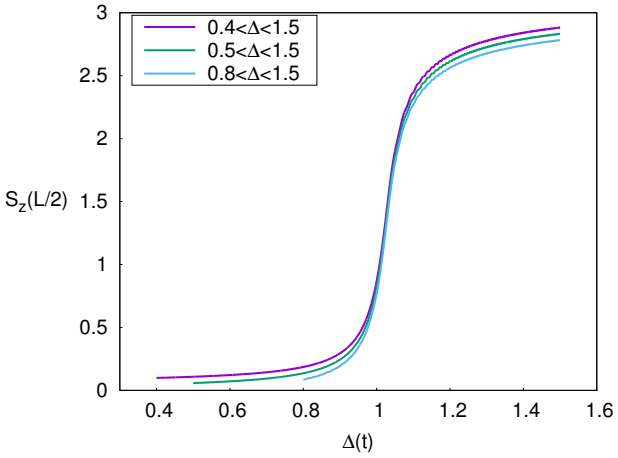

(b) *Half-chain magnetisation.*

Figure 5.5: Dynamic simulations in different ranges of time quenches: $0.4 < \Delta(t) < 1.5$, $0.5 < \Delta(t) < 1.5$ and $0.8 < \Delta(t) < 1.5$.

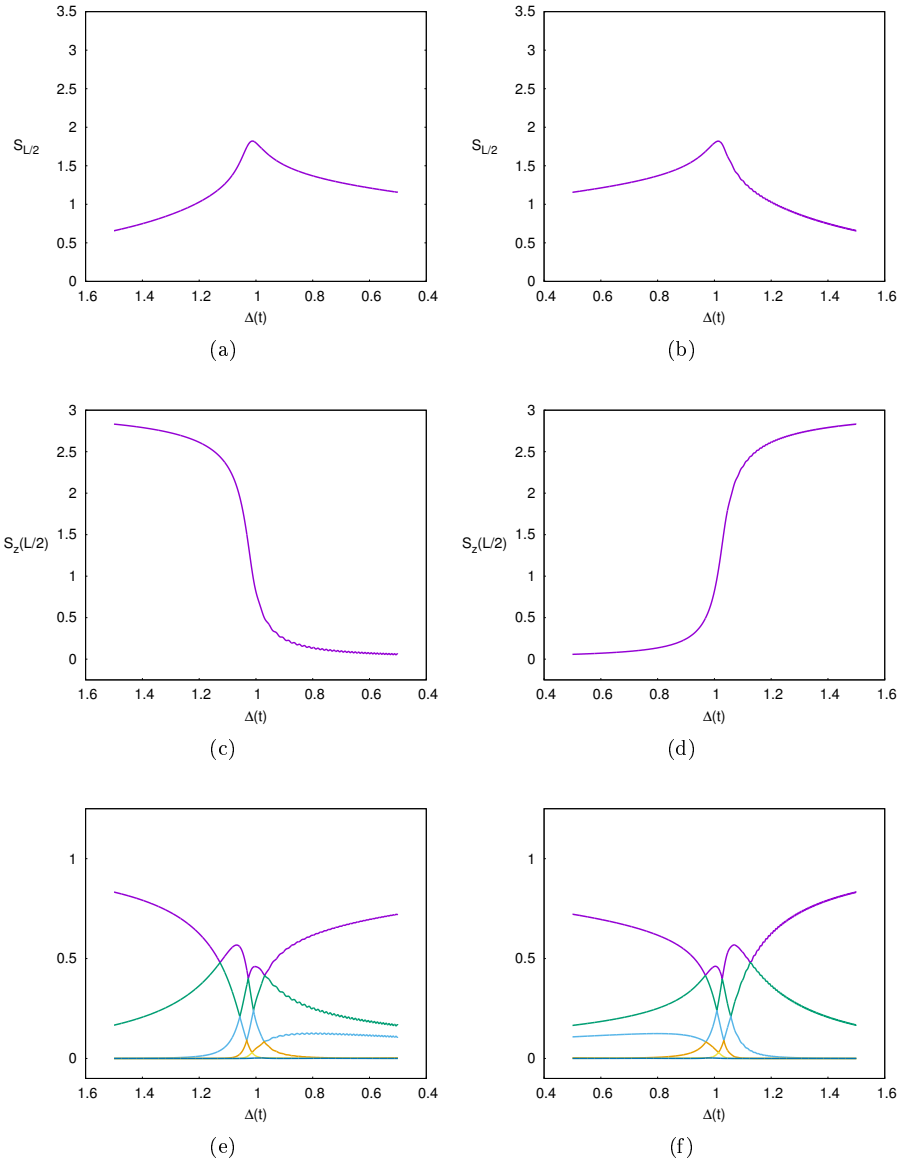

Figure 5.6: Entanglement entropy (top row), half-chain magnetisation (middle row) and entanglement spectrum (bottom row) for an adiabatic quench from $\Delta = 1.5$ to 0.5 (left column) and viceversa (right column).

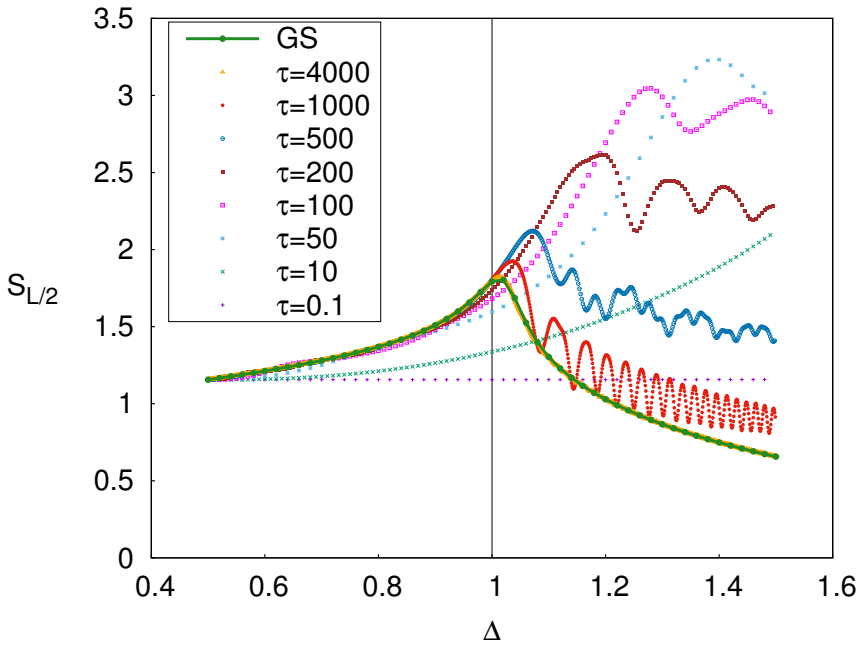

Figure 5.7: Dynamics of the entanglement entropy for $L = 12$ and for different values of τ. Vertical line marks the location of the quantum critical point.

5.0.2 Comparative analysis

In Figs. 5.7 and 5.8 the dynamics of entanglement entropy and half-chain magnetisation for different quench regimes are considered. We begin our analysis with the nearly instantaneous quenches, characterised by small values of quench times, such as $\tau = 0.1$ in the plots. The dynamics of both observables is essentially frozen. The ground state of the system cannot follow the sudden changes the Hamiltonian experiences: as a result, both entanglement entropy and half-chain magnetisation do not change at all. The initial state, which is the fundamental one in the paramagnetic region, cannot follow the abrupt evolution of the Hamiltonian and becomes an excited state in the ferromagnetic phase.

As the values of τ grow, a wide intermediate regime is encountered, marked by oscillations in both entropy and magnetisation. Starting from the faster sweeps, i.e. curves with $\tau = 10$ and 50, we see that near the quantum critical point the entanglement entropy increases linearly. This evidence can be related to the already mentioned conformal field theory (see Sec. 3.3 along with its references): in that context, Calabrese and Cardy showed [7] that the entanglement entropy is predicted to grow linearly, at least in the first part of its evolution, with a slope related to the central charge corresponding to the underlying conformal field theory. This behaviour have been confirmed for the Ising model in

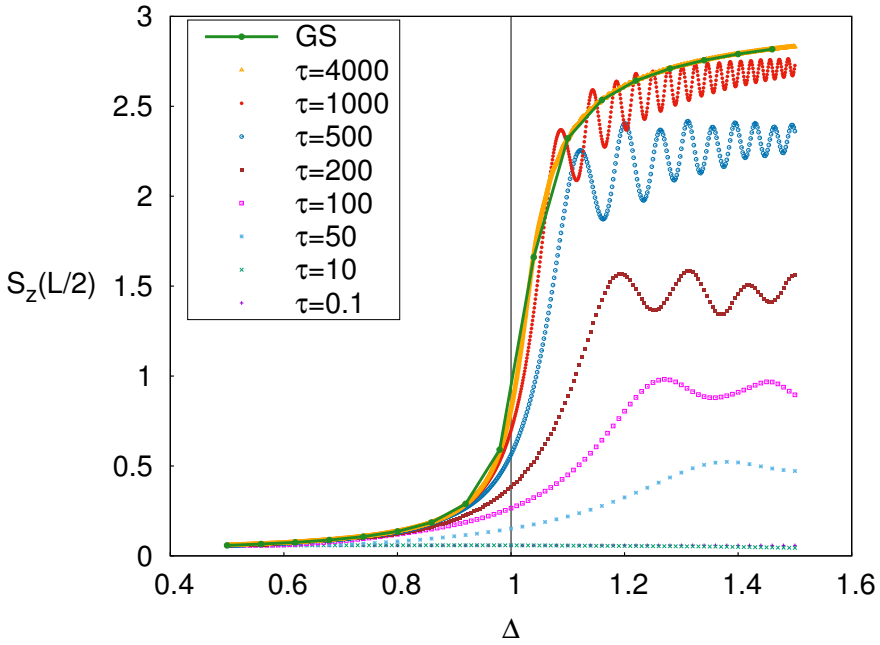

Figure 5.8: Dynamics of the half-chain magnetisation for $L = 12$ and for different values of τ. Vertical line marks the location of the quantum critical point.

[9], where this picture has been applied quantitatively. In this preliminar work we only have a qualitative approach.

Spins in this intermediate regime begin to order, with the developement of a net magnetisation after the critical point. However, we note that this observable is less sensitive to quench time variations than entanglement entropy. For instance, considering the curve with $\tau = 10$, it is clear that its magnetisation is still null despite the growth of entropy. To understand this result we must turn our attention to the microscopic dynamics: we already mentioned in the static case that the paramagnetic ground state, as well as its first excited states, is characterised by zero magnetisation on every length scale: indeed, as Fig. 5.9(a) shows, in this region not only its mean value, but also the single-site magnetisation is approximately null. We saw that in fast quenches the initial ground state cannot evolve at all, hence remaining steady during all evolution. When the quench times become larger, the system can access to its first excited states, that begin to superimpose in order to form the new state managing to follow the varying Hamiltonian. This process, as Δ increases, gradually involves more states with zero net magnetisation, but half-chain ordering. Consequently to this merge, the ground state smoothly gains a net half-chain magnetisation. As a matter of fact, in the ferromagnetic region the situation is opposite, as we can see in Fig. 5.9(b): the ground state and first excited states display half-

chain ferromagnetic alignement, oppositely to the highest-energy states whose single-site magnetisation is approximately zero.

After, we consider slower sweeps, with $\tau = 100 \div 1000$. While in the first part of the evolution the curves still linearly increase, towards the end an oscillatory behaviour stabilises for both entropy and magnetisation. This oscillations were already observed in ref. [9] and have been ascribed to a superposition of excited states of the instantaneous Hamiltonian the system ends up into, after passing the quantum critical point. As the quench time grows, the oscillation frequency becomes higher. The incostant pattern of the curves may suggest that we are effectively dealing with a superposition of different frequencies, at least in some cases.

Finally, we consider the quasi-adiabatic quench, i.e. the curves for $\tau = 4000$. The entanglement entropy and magnetisation follow closely the static value. This behaviour was already encountered in [9], and can be ascribed to the adiabatic theorem: in fact due to its finite size, provided a sufficiently large τ, it is possible for the system to reach the adiabatic limit. A motivation can also be found from a dynamical point of view: in this case the relaxation time is far smaller than the variation scale of the Hamiltonian. For this reason, defects, i.e. excitations of the system due to the change in the Hamiltonian, can form and relax before a new variation happens. Consequently, the static ground state is followed.

Figs. 5.10 and 5.11 show the values corresponding to the first maximum in the evolution of entanglement entropy and half-chain magnetisation as a function of the quench time. Both curves are extremely smooth and show a regular behaviour, to a certain extent. We do not attempt an equation fitting, because of the low number of points gathered. Anyway, as a future goal, achieving the fit would allow to better describe the dynamic evolution of the model. Indeed, we recall that according to the KZ physics (seemingly behind this process) entanglement entropy as well as order parameters (such as $S_z(L/2)$) should show a power-law decay with universal exponents.

At the end of this analysis, we turn our attention to the dynamics of defects formation. The results found are interesting in relation to the Kibble-Zurek mechanism. Indeed, the core of the KZM description is focused on the evaluation of such defect density. The developement of a different order in a system experiencing a quantum phase transition is prompted by these defects: they enucleate in some position in the system and gradually expand to form domains of different order. This process continues on a growing scale until the new phase is set up. All the previous considerations can be visually summarized in Figs. 5.12, 5.13 and 5.14: the three plots display the magnetisation of all 12 sites of the chain as a function of the anisotropy parameter in a dynamic

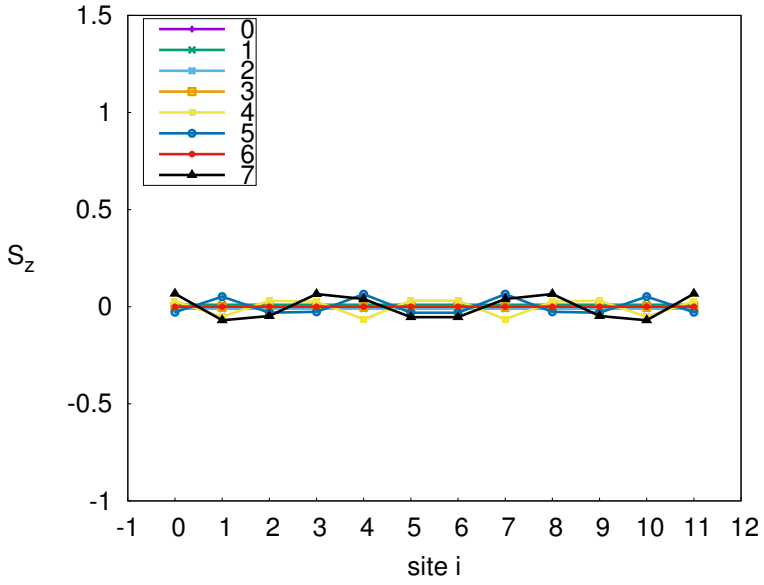

(a) $\Delta = 0.50$.

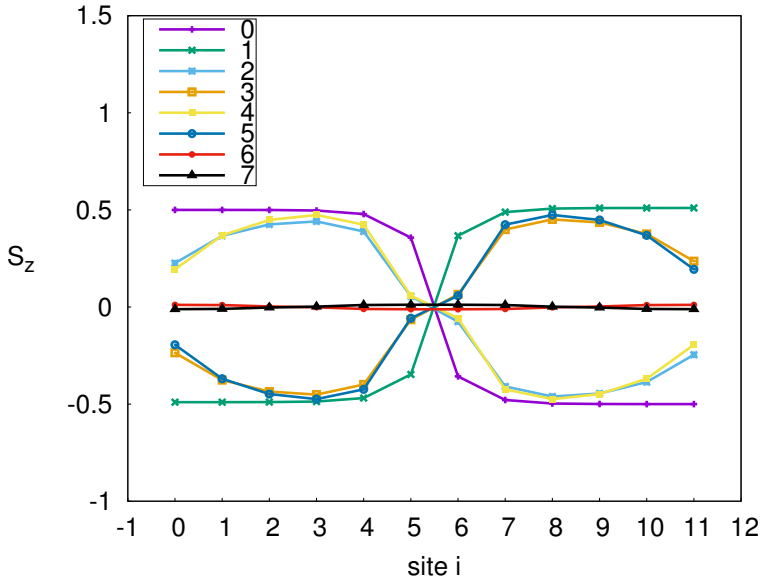

(b) $\Delta = 1.50$.

Figure 5.9: Single-site magnetisation of the first 8 energy levels in static simulations with fixed Δ. '0' marks the lowest-energy state.

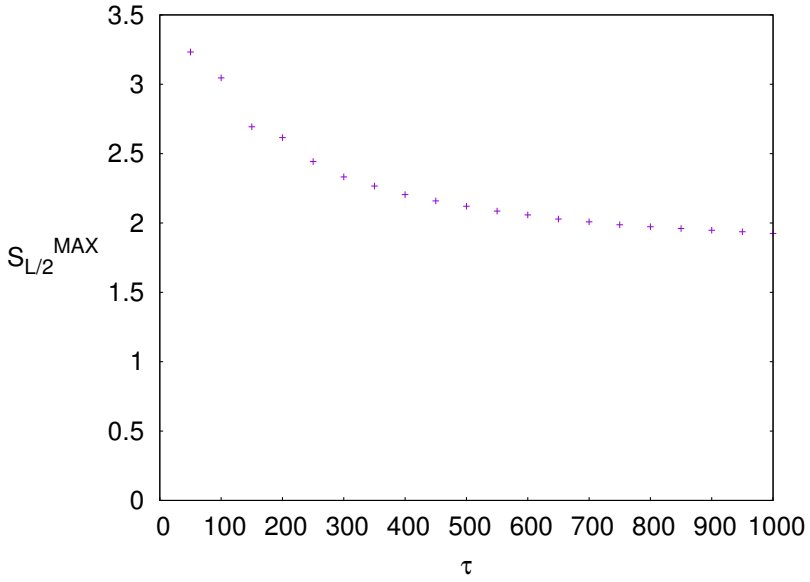

Figure 5.10: First maximum in entanglement entropy as a function of the quench time τ.

evolution with $\tau = 10$, 500 and 4000. On the base of each plot we show a contour plot reporting the value of the magnetisation S_z. In this way the dynamic ordering becomes evident for the whole chain. When quench times are large, the initial state can adiabatically follow the instantaneous ground state. Hence, in this case the defect consists in a spin alignement kink becoming more and more favoured as the ferromagnetic phase is reached. Eventually, the system ends up in a configuration maximizing the exchange energy as well as keeping a total null magnetisation: this state is composed of 6 spins pointing up and 6 pointing down. On the opposite situation, no evolution happens and the spins on each site remain approximately zero for all the duration of the sweep. For the intermediate regime, oscillations superimpose to a general ordering of half the chain.

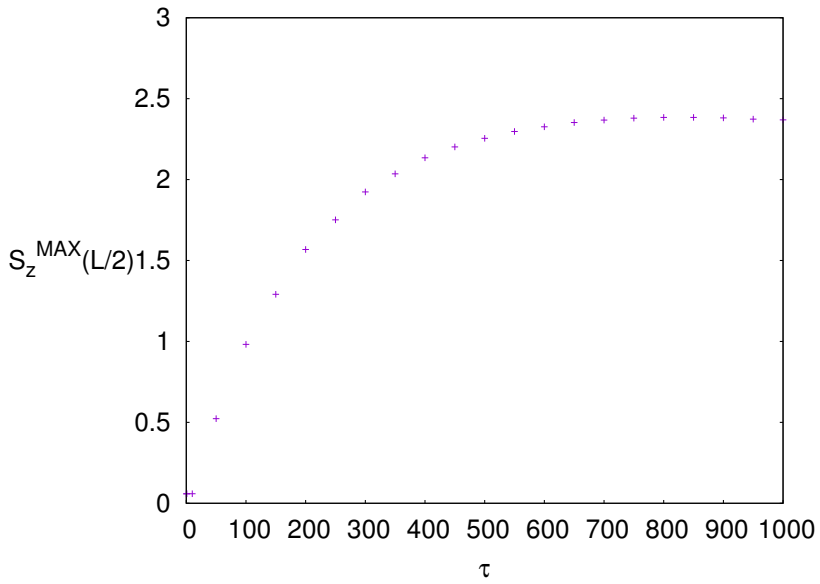

Figure 5.11: First maximum in half-chain magnetisation as a function of the quench time τ.

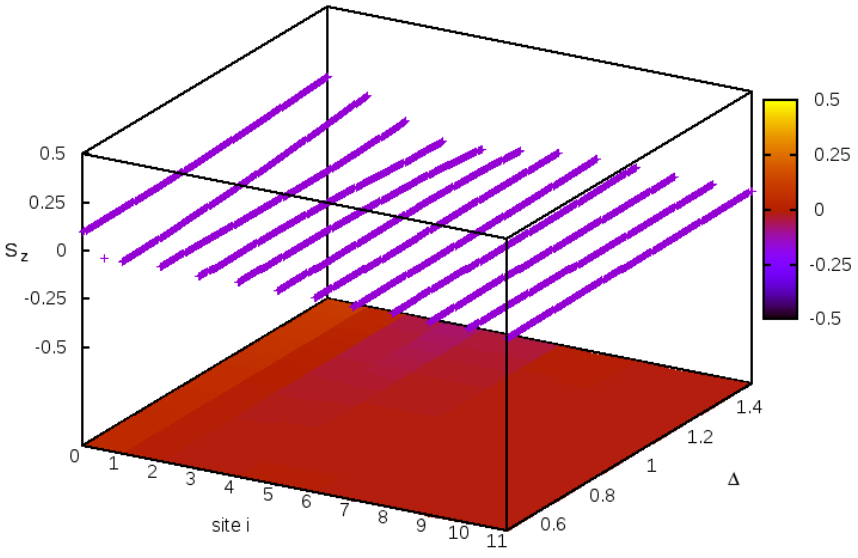

Figure 5.12: Dynamics of single-site magnetisation as a function of Δ and for $\tau = 10$.

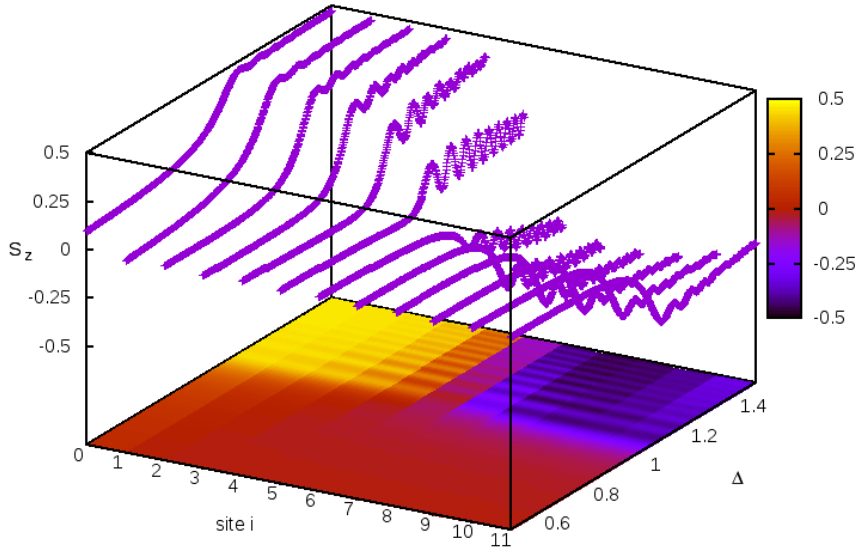

Figure 5.13: Dynamics of single-site magnetisation as a function of Δ and for $\tau = 500$.

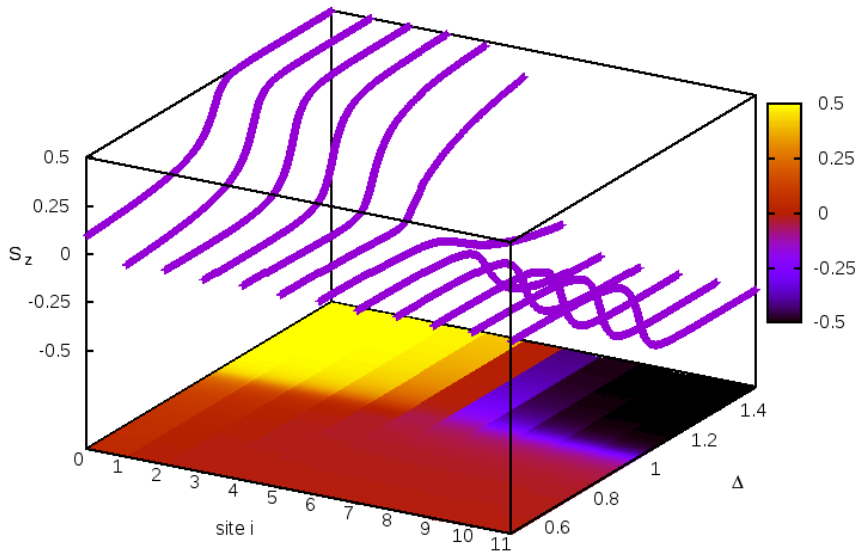

Figure 5.14: Dynamics of single-site magnetisation as a function of Δ and for $\tau = 4000$.

Chapter 6

Conclusions and Outlooks

In this thesis we presented a model to describe the dynamics of a quantum phase transition in a non-interacting quantum system, and performed a similar analysis on the fully interacting Heisenberg XXZ chain.

In particular, we concentrated on the ferromagnetic critical point $\Delta = 1$ and simulated a transition from the paramagnetic to the ferromagnetic phase via tDMRG with different quench times τ, using numerical analysis to dynamically evaluate entanglement entropy, half-chain magnetisation and entanglement spectrum.

The results highlight the existence of three τ- dependent regimes of behaviour: on one hand, with instantaneous quenches, the initial state of the system does not evolve according to the Hamiltonian and the dynamics is essentially frozen. In the opposite situation, with quasi-adiabatic quenches, the fundamental state evolution follows the real instantaneous ground state. Hence, we observe for example the gradual development of a net magnetisation during the transition towards the ferromagnetic region. The intermediate regime is charachterised by oscillations in entropy and magnetisation, induced by the pronounced oscillating pattern of the density-matrix eigenvalues. These three behaviours, seeming physically reasonable, suggest that the considered observables can properly characterize quantum phase transitions in such an interacting model.

As a future work, it would be interesting to focus on the research of universal scaling laws related to dynamical quantities, which would highlight some transition details as already accomplished, e.g., in the Ising model. The regularity of our scaling plots is extremely promising, though more complete data are needed to try a fit.

There are several direction our research could be developed towards. Firstly, it would be interesting to study the XXZ model across the antiferromagnetic

critical point. This requires longer simulations, since the related energy gap opens up very slowly. In all cases, it i necessary to study the scaling in the thermodynamic limit. This goal can be achieved working with chains with a higher number of sites. Nevertheless, this limit is not necessarily huge: for these simple models it usually settles under one hundred (e.g., for the Ising model $L = 40$ is sufficient) sites.

Moreover, a generalisation should also include the case of full anisotropy along the three axes, i.e. the XYZ model. In the latter case, further symmetry variations occour in the Hamiltonian (for example, magnetisation is no longer a conserved quantity) that would be interesting to consider.

Finally, a intriguing issue concerns the defect formation we only glimpsed in the last part of our work. It would be of major interest to describe the evolution of these defects quantitatively. To attain this aim, one should target not only the ground state but also some excited states already exhibiting a defect profile and investigate their dynamics.

Bibliography

[1] L. Amico, R. Fazio, A. Osterloh, and V. Vedral, *Entanglement in Many-Body Systems*, Rev. Mod. Phys., 80 (2008), p. 517.

[2] R. J. Baxter, *One-dimensional anisotropic Heisenberg chain*, Ann. Phys., 70 (1972), p. 323.

[3] ——, *Partition function of the Eight-Vertex lattice model*, Ann. Phys., 70 (1972), p. 193.

[4] J. Bell, *Speakable and unspeakable in Quantum Mechanics*, Cambridge University Press, 1987.

[5] H. Bethe, *Zur Theorie der Metalle I. Eigenwerte und Eigenfunktionen der linearen Atomkette*, Z. Phys., 71 (1931), p. 205.

[6] P. Calabrese and J. Cardy, *Entanglement entropy and quantum field theory*, J. Stat. Mech., (2004), p. P06002.

[7] ——, *Entanglement entropy and conformal field theory*, J. Phys. A: Math. Theor., 42 (2009), p. 504005.

[8] T. Caneva, R. Fazio, and G. Santoro, *Adiabatic quantum dynamics of a random Ising chain across its quantum critical point*, Phys. Rev. B, 76 (2007), p. 144427.

[9] E. Canovi, E. Ercolessi, P. Naldesi, L. Taddia, and D. Vodola, *Dynamics of entanglement entropy and entanglement spectrum crossing a quantum phase transition*, Phys. Rev. B, 89 (2014), p. 104303.

[10] L. Cincio, J. Dziarmaga, M. Rams, and W. H. Zurek, *Entropy of entanglement and correlations induced by a quench: Dynamics of a quantum phase transition in the quantum Ising model*, Phys. Rev. A, 75 (2007), p. 052321.

[11] G. De Chiara, S. Montangero, P. Calabrese, and R. Fazio, *Entanglement entropy dynamics of Heisenberg chains*, J. Stat. Mech., (2006), p. P03001.

[12] A. del Campo and W. H. Zurek, *Universal of phase transition dynamics: Topological defects from symmetry braking*, Int. J. Mod. Phys. A, 29 (2014), p. 1430018.

[13] J. des Cloizeaux and J. Pearson, *Spin-Wave Spectrum of the Antiferromagnetic Linear Chain*, Phys. Rev., 128 (1962), p. 2131.

[14] J. Dziarmaga, *Dynamics of a quantum phase transition and relaxation to a steady state*, Adv. Phys., 59 (2010), p. 1063.

[15] A. Einstein, B. Podolsky, and N. Rosen, *Can quantum-mechanical description of physical reality be considered complete?*, Phys. Rev., 47 (1935), p. 777.

[16] J. Eisert, M. Cramer, and M. B. Plenio, *Area laws for the entanglement entropy - a review*, Rev. Mod. Phys., 82 (2010), p. 277.

[17] V. Eisler and Z. Zimborás, *Entanglement in the XX spin chain and energy current*, Phys. Rev. A, 71 (2005), p. 042318.

[18] M. Fagotti, M. Collura, F. Essler, and P. Calabrese, *Relaxation after quantum quenches in the spin-1/2 Heisenberg XXZ chain*, Phys. Rev. B, 89 (2014), p. 125101.

[19] M. Fagotti and F. Essler, *Stationary behaviour of observables after a quantum quench in the spin-1/2 Heisenberg XXZ chain*, J. Stat. Mech., (2013), p. P707012.

[20] K. Hallberg, *New trends in density matrix renormalization*, Advances in Physics, 55 (2006), p. 477.

[21] W. Heisenberg, *Zur Theorie des Ferromagnetismus*, Z. Phys., 49 (1928), p. 619.

[22] L. Hulten, *Uber has Austauschproblem eines Kristalls*, Ark. Mat. Astron. Fys., A26 (1938), p. 1.

[23] A. R. Its, B.-Q. Jin, and V. E. Korepin, *Entanglement in the XY spin chain*, J. Phys. A: Math. Gen., 38 (2005), p. 2975.

[24] B.-Q. Jin and V. E. Korepin, *Quantum Spin Chain, Toeplitz Determinants and Fisher-Hartwig Conjecture*, J. Stat. Phys., 116 (2004), p. 79.

[25] N. Laflorencie, *Scaling of entanglemen entropy in the random singlet phase*, Phys. Rev. B, 72 (2005), p. 140408(R).

[26] C. Lanczos, *An iteration method for the solution of the eigenvalue problem of linear differential and integral operator*, J. Res. Natl. Bur. Stand., 45 (1950), p. 225.

[27] J. I. Latorre and A. Riera, *A short review on entanglement in quantum spin systems*, J. Phys. A: Math. Theor., 42 (2009), p. 504002.

[28] G. Morandi, F. Napoli, and E. Ercolessi, *Statistical Mechanics: an Intermediate Course*, World Scientific, 2001.

[29] M. A. Nielsen and I. L. Chuang, *Quantum Computation and Quantum Information*, Cambridge University Press, 2000.

[30] R. M. Noack and S. R. Manmana, *Diagonalization- and Numerical Renormalization-Group-Based Methods for Interacting Quantum Systems*, in AIP Conf. Proc., vol. 789, 2005, p. 93.

[31] F. Pellegrini, S. Montangero, G. Santoro, and R. Fazio, *Adiabatic quenches through an extended quantum critical region*, Phys. Rev. B, 77 (2008), p. 140404(R).

[32] I. Peschel, *On the entanglement entropy for an XY spin chain*, J. Stat. Mech., (2004), p. P12005.

[33] I. Peschel, X. Wang, M. Kaulke, and K. Hallberg, eds., *Density-Matrix Renormalization, A New Numerical Method in Physics*, Lecture Notes in Physics, Springer, Berlin, 1999.

[34] A. Polkovnikov, K. Sengupta, A. Silva, and M. Vengalattore, *Nonequilibrium dynamics of closed interacting quantum systems*, Rev. Mod. Phys., 83 (2011), p. 863.

[35] W. H. Press, S. A. Teukolsky, W. T. Vetterling, and B. P. Flannery, *Numerical Recipes in C++*, Cambridge University Press, 2nd ed., 1993.

[36] S. Sachdev, *Quantum Phase Transitions*, Cambridge University Press, 2011.

[37] U. Schollwöck, *The density-matrix renormalization group*, Rev. Mod. Phys., 77 (2005), p. 259.

[38] E. Schrödinger, *Discussion of probability relations between separated systems*, Proc. Cambridge Phil. Soc., 31 (1935), p. 555.

[39] G. Torlai, L. Tagliacozzo, and G. De Chiara, *Dynamics of the entanglement spectrum in spin chains*, J. Stat. Mech., (2014), p. P06001.

[40] S. R. White, *Density Matrix Formulation for Quantum Renormalization Groups*, Phys. Rev. Lett., 69 (1992), p. 2863.

[41] S. R. White and R. Noack, *Real-space quantum renormalization groups*, Phys. Rev. Lett., 68 (1992), p. 3487.

[42] K. G. Wilson, *The renormalization group: Critical phenomena and the Kondo problem*, Rev. Mod. Phys., 47 (1975), p. 773.

[43] C. N. Yang and C. P. Yang, *One-Dimensional Chain of Anisotropic Spin-Spin Interactions. I. Proof of Bethe's Hypothesis for Ground State in a Finite System*, Phys. Rev., 150 (1966), p. 321.

[44] ——, *One-Dimensional Chain of Anisotropic Spin-Spin Interactions. II. Properties of the Ground-State Energy per Lattice Site for an Infinite System*, Phys. Rev., 150 (1966), p. 327.

[45] ——, *One-Dimensional Chain of Anisotropic Spin-Spin Interactions. III. Applications*, Phys. Rev., 151 (1966), p. 258.